Research Square

Preprints are preliminary reports that have not undergone peer review.
They should not be considered conclusive, used to inform clinical practice,
or referenced by the media as validated information.

Therapy-induced senescence mitochondrial proteome reveals a role for ABAT in catabolic reprogramming

Jennyfer Martínez
Universidad de la República
Doménica Tarallo
Universidad de la República
Alejandro Leyva
Instituto de Investigaciones Biológicas Clemente Estable (IIBCE), Montevideo, Uruguay, Unidad mixta de Bioquímica y Proteómica Analíticas
Rodrigo Martino-Kunsch
Universidad de la República
Inés Marmisolle
Universidad de la República
Rafael Sebastián Fort
Universidad de la República
Marcos Tassano
Universidad de la República
Carolina Perroni
Universidad de la República
Guillermo Grünwaldt
Universidad de la República
Gabriel Anderson
Universidad de la República
Andrés López-Radcenco
Universidad de la República
Guillermo Moyna
Universidad de la República
Ernesto Miquel
Universidad de la República
Juan Pablo Gambini
Universidad de la República
Paula Céspedes
Institut Pasteur de Montevideo

Mariela Bollati-Fogolín
Institut Pasteur de Montevideo
Natalia Isla
Lorraine University, CNRS UMR 7365
María Ana Duhagon
Universidad de la República
Mercedes Rodríguez-Teja
Universidad de la República
María Moreno
Universidad de la República
Rosario Durán
Instituto de Investigaciones Biológicas Clemente Estable (IIBCE), Montevideo, Uruguay, Unidad mixta de Bioquímica y Proteómica Analíticas
Celia Quijano
celia.quijano@gmail.com

Universidad de la República

Article

Keywords:

Posted Date: November 25th, 2026

DOI: https://doi.org/10.21203/rs.3.rs-11650772/v1

License: This work is licensed under a Creative Commons Attribution 4.0 International License.
Read Full License

Additional Declarations: No competing interests reported.

Therapy-induced senescence mitochondrial proteome reveals a role for ABAT in catabolic reprogramming

Jennyfer Martínez[1], Doménica Tarallo[1], Alejandro Leyva[2], Rodrigo Martino-Kunsch[3], Inés Marmisolle[1], Rafael Sebastián Fort[4], Marcos Tassano[5], Carolina Perroni[5], Guillermo Grünwaldt[1], Gabriel Anderson[6], Andrés López-Radcenco[6], Guillermo Moyna[6], Ernesto Miquel[7], Juan Pablo Gambini[8], Paula Céspedes[9,10], Mariela Bollati-Fogolín[9], Natalia de Isla[11], María Ana Duhagon[12], Mercedes Rodríguez-Teja[3], María Moreno[13], Rosario Durán[2] and Celia Quijano[1].

[1] Departamento de Bioquímica, Facultad de Medicina, and Centro de Investigaciones Biomédicas (CEINBIO), Universidad de la República, Uruguay
[2] Unidad mixta de Bioquímica y Proteómica Analíticas. Institut Pasteur de Montevideo and Instituto de Investigaciones Biológicas Clemente Estable (IIBCE), Uruguay
[3] Departamento de Genética, Facultad de Medicina, Universidad de la República, Uruguay
[4] Sección Genómica Funcional, Facultad de Ciencias, Universidad de la República, Uruguay
[5] Departamento de Radiofarmacia, Centro de Investigaciones Nucleares, Facultad de Ciencias, Universidad de la República, Uruguay
[6] Laboratorio de Química Orgánica, Departamento de Química del Litoral, CENUR Litoral Norte, Universidad de la República, Uruguay
[7] Departamento de Histología y Embriología, Facultad de Medicina, Universidad de la República, Uruguay
[8] Centro Uruguayo de Imagenología Molecular and Centro de Medicina Nuclear, Hospital de Clínicas, Facultad de Medicina, Universidad de la República, Uruguay
[9] Unidad de Biología Celular, Institut Pasteur de Montevideo, Uruguay
[10] Present Address: Advanced Bioimaging Unit, Institut Pasteur de Montevideo and Universidad de la República, Uruguay.
[11] Lorraine University, CNRS UMR 7365, IMoPA laboratory, 54500 Vandoeuvre-lès-Nancy, France.
[12] Sección Genómica Funcional, Facultad de Ciencias and Departamento de Genética, Facultad de Medicina, Universidad de la República, Uruguay
[13] Laboratorio de Vacunas Recombinantes, Unidad Académica de Desarrollo Biotecnológico, Facultad de Medicina, Universidad de la República, Uruguay

* Correspondence should be addressed to: Celia Quijano, email: celiq@fmed.edu.uy; celia.quijano@gmail.com

Abstract

Genotoxic agents used for cancer treatment activate the DNA damage response and can induce apoptosis and/or cellular senescence in tumor cells. This state is characterized by irreversible proliferation arrest mediated by the p53/p21 pathway and a senescence-associated secretory phenotype (SASP) that influences tumor progression and treatment response.

The methylating chemotherapeutic agent temozolomide (TMZ) can induce cellular senescence and promote mitochondrial biogenesis in melanoma. In this work, we characterized the mitochondrial proteome of TMZ-induced senescent melanoma B16-F1 cells using shotgun proteomics. We identified a significant increase in enzymes associated with lipid and amino acid catabolism, the tricarboxylic acid (TCA) cycle, the respiratory chain, and oxidative phosphorylation. Consistent with these findings, intracellular metabolomic analysis revealed decreases in several amino acids, supporting changes in nutrient utilization in senescent cells.

Among the proteins increased in senescent cells, we identified 4-aminobutyrate aminotransferase (ABAT), a mitochondrial enzyme involved in γ-aminobutyric acid (GABA) and α-ketoglutarate conversion to succinic semialdehyde and glutamate, which can fuel the TCA cycle. Abat KO decreased mitochondrial respiration and compromised the viability of senescent melanoma cells under nutrient-restricted culture conditions. Mitochondrial mass and Abat expression were also increased in senescent melanoma cells induced by the radionuclide 223Ra, as well as in tumors of mice treated with dacarbazine. Finally, p53 silencing decreased Abat expression and mitochondrial oxygen consumption rates, whereas p53 stabilization increased Abat expression.

These findings support that senescence increases metabolic flexibility of melanoma cells, expanding the range of substrates and mitochondrial catabolic pathways that can sustain energy demands, and suggest that p53 contributes to the regulation of metabolic reprogramming in therapy-induced senescence.

Introduction

Cellular senescence is triggered by different stress stimuli, including telomere attrition; DNA damage by oxidants, chemotherapeutics, or radiation; or strong mitogenic signals, such as

oncogene expression[1]. Activation of the DNA damage response (DDR) pathway, which involves phosphorylation of ATM or ATR kinases, leads to cell-cycle arrest mediated by the p53/p21/pRB or p16/pRB pathways. This also includes the formation of DNA damage nuclear foci (e.g., γH2AX foci), heterochromatin foci (SAHFs), and the acquisition of a senescence-associated secretory phenotype (SASP). Senescent cells also present morphological changes, an increase in lysosomal mass, and enhanced oxidative metabolism[2].

Senescence activation acts as a barrier to cancer development, and neoplastic transformation involves evasion of senescence. However, cancer cells can also enter a senescent state upon exposure to several anticancer therapies[3]. Chemotherapeutic agents, such as methylating agents, topoisomerase inhibitors, cell cycle inhibitors, and telomerase inhibitors, as well as radiation, can induce senescence in tumor and non-tumor cells. This process is known as therapy-induced senescence (TIS) and can strongly impact the response to treatment and the development of the disease[4,5]. Senescent cells secrete growth factors, cytokines, proteases, and other factors that can be beneficial or deleterious for the organism[5]. Factors secreted by senescent cells can reinforce senescence, recruit immune cells, and promote inflammation, cell proliferation, and angiogenesis, among other effects[6]. Accumulation of senescent cells has been associated with tumor recurrence[7] and with the side effects of different cancer therapies[8]. Besides, senescent cells can be found in skin ulcerations caused by radiotherapy and in fibrotic events in skin and lung tissue following chemo- and radiotherapy[9,10].

Recent studies show that profound metabolic alterations accompany senescence. Our group and others have found evidence of a significant increase in mitochondrial biogenesis and oxidative metabolism in TIS or oncogene-induced senescence (OIS)[11–14]. Inhibition of glucose, pyruvate, and lipid metabolism can induce apoptosis in senescent cells or alter the SASP[11,12,15–18]. Moreover, cytosolic mtDNA and double-stranded mtRNA, as well as citrate and acetyl-CoA, have been identified as key signaling molecules in SASP establishment[19–22]. Therefore, enzymes and transcription factors involved in mitochondrial metabolism and biogenesis appear to be promising targets for modulating the SASP.

To identify the pathways supporting metabolic reprogramming in TIS, we performed shotgun proteomics on mitochondria-enriched subcellular fractions and measured intracellular metabolites in senescent and non-senescent melanoma cells. We found increased levels of enzymes from lipid

and amino acid catabolic pathways, the respiratory chain, and oxidative phosphorylation in senescent B16-F1 melanoma cells, along with decreased levels of some amino acids. Among these, we identified and validated a significant increase in 4-aminobutyrate aminotransferase (ABAT) expression and levels. This enzyme catalyzes the conversion of γ-aminobutyric acid (GABA) to succinate, a tricarboxylic acid (TCA) cycle intermediate. Besides, we explored whether the increase in mitochondrial catabolism in senescent cells was regulated by p53[23,24]. This transcription factor is a known effector of the senescent phenotype, but also promotes the expression of proteins involved in the assembly of respiratory complexes[25,26], replication, transcription, and translation of mtDNA[27,28], and can translocate to mitochondria, where it interacts with proteins involved in mtDNA maintenance and expression[29,30]. Overall, our results provide a proteomic and metabolic map of catabolic pathways in senescent melanoma cells, highlighting increased dependence and flexibility in mitochondrial oxidative metabolism. As well as supporting a role for p53-dependent *Abat* expression in mitochondrial bioenergetic adaptations.

Results

Mitochondrial proteome of therapy-induced senescent melanoma cells

We established a therapy-induced senescence model by exposing B16-F1 melanoma murine cells to temozolomide (TMZ), using vehicle-treated (DMSO) cells as the control condition (Control). Our group previously characterized this model by measuring several senescence markers, as reported in Martínez et al., 2019[14]. TMZ treatment results in a culture with a high percentage of senescent cells, as shown by the senescence associated-β-galactosidase (SA-β-gal) activity assay (Fig. 1a). Analysis of mitochondria after staining with MitoTracker Green FM showed mitochondrial elongation (Fig. 1b) and a 2.5-fold increase in mitochondrial mass (Fig. 1c). Similarly, mtDNA/nDNA was 4 times higher in senescent than control cells (1.0 ± 0.1 vs 4 ± 0.6, $n = 3$, $P < 0.001$). In addition, functional analysis of oxygen consumption rate revealed increases in all mitochondrial respiratory parameters in senescent cells compared with control cells (Fig. 1d). Notably, senescent cells showed a 9.8-fold increase in maximum respiration rate, exceeding the increases in mitochondrial mass and mtDNA/nDNA. Together, these results confirm that acquisition of a senescent phenotype in TMZ-treated B16-F1 cells is accompanied by increased

mitochondrial mass, elongation, and respiration, and suggest that increased electron transport chain activity is not solely due to higher mitochondrial content associated with cell enlargement.

We then studied cell bioenergetics with the SCENITH method, which measures protein synthesis in the absence and presence of metabolic inhibitors[31]. Protein synthesis was slightly lower in senescent cells than in non-senescent cells, and the signal was abolished by the translation initiation inhibitor harringtonine (H) (Fig. S1a-b). We confirmed that senescent cells, but not control cells, depend on mitochondrial metabolism for protein synthesis since it was inhibited by oligomycin (Oligo), an ATP synthase inhibitor (Fig. 1e and 1f). Protein synthesis in control cells was highly dependent on glucose, as shown by inhibition with the hexokinase inhibitor 2-deoxy-glucose (DG) (Fig. 1e). This was not observed in senescent cells (Fig. 1e), suggesting that glucose might not be the only nutrient serving as an energy source.

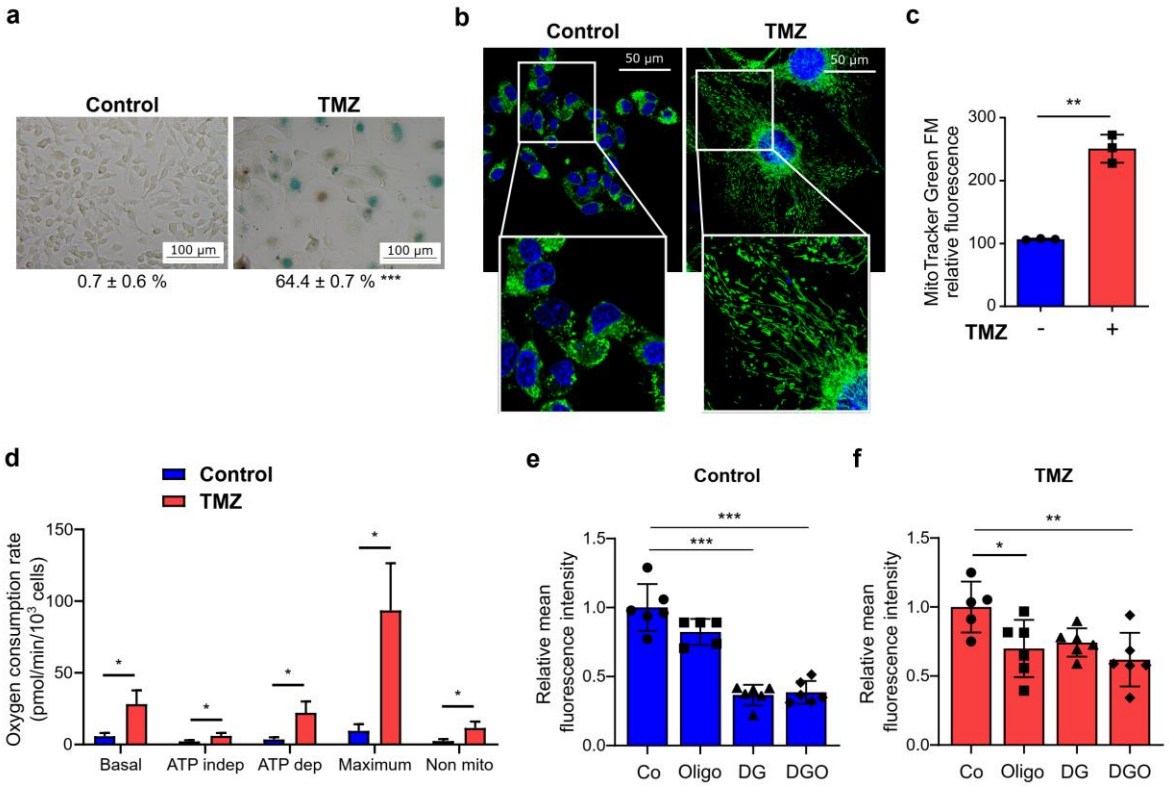


Figure 1. Senescence induction in mouse melanoma cells. B16-F1 cells were exposed to TMZ (200 µM) to induce senescence or to DMSO (Control) (two 5-hour incubations separated by 24 hours) and evaluated four days after the second exposure. **a** Representative images of the SA-β-gal activity assay. The percentage of SA-β-gal-positive cells after TMZ treatment is shown for each condition (n = 3). **b** and **c** Cells were stained with MitoTracker Green FM (green) and Hoechst 33342 (blue) and analyzed by confocal microscopy (**b**) or by flow cytometry after cells were collected by trypsinization, and the relative geometric mean fluorescence intensity is shown in (**c**) (n = 3-4). **d** Respiratory parameters obtained from oxygen consumption rate (OCR) measurements before and following the sequential addition of oligomycin, FCCP, and antimycin A/rotenone (n = 4-5). **e** and **f** Cells were incubated with oligomycin (Oligo, 1 µM), 2-deoxyglucose (DG, 100 mM), or a mixture of oligomycin plus 2-deoxyglucose (DGO) to assess glucose dependence and mitochondrial dependence of protein synthesis. Puromycin was added (10 µg/ml) at the end of the incubation with the inhibitor, and translation was assessed by measuring puromycin incorporation into proteins by flow cytometry. Mean fluorescence intensity of control (**e**) and senescent (**f**) cells is shown relative to the condition without inhibitors (Co) (n = 5-6). Results are the mean ± S.D. In **a**, **c** and **d**, t-tests were performed. In **e** and **f** we determined statistical differences by one-way ANOVA and Dunnett's post hoc for multiple comparisons. * $P < 0.05$, ** $P < 0.001$, *** $P < 0.0001$.

To better understand the molecular events underlying this metabolic reprogramming, we performed shotgun proteomics on mitochondria-enriched fractions from senescent and non-senescent cells. To do this, we obtained subcellular fractions by differential centrifugation and confirmed enrichment of succinate dehydrogenase subunit A (SDHA, a mitochondrial protein) in mitochondrial fractions compared with cell lysates in both senescent and non-senescent cells by western blot (Fig. 2a and 2b). We subjected proteins from mitochondria-enriched fractions to in-gel trypsin digestion and analyzed peptides by nano-HPLC coupled to a mass spectrometer. Principal Component Analysis (PCA) showed the four biological replicates of each condition clustered, confirming the consistency of the changes observed upon induction of senescence (Fig. 2c). We identified 1337 proteins present in the four control replicates and 1518 proteins present in the four TMZ-treated samples with at least two peptides per protein (Data_file S1). Using EnrichR and the Gene Ontology Cellular Components database, we confirmed a significant enrichment in proteins localized to mitochondrial membranes and the matrix in both conditions assessed (Data_file S2).

Using the Venn diagram statistical module in PatternLab, we identified 47 proteins present exclusively in mitochondrial fractions of Control cells and 114 proteins in mitochondrial fractions of TMZ-treated cells (Fig. 2d, Data_file S3). To detect differences in protein levels, we used the PatternLab TFold module and identified 601 differentially abundant proteins with a Benjamini–Hochberg (BH)-adjusted P-value < 0.05 (Fig. 2e, blue data in Data_file S4).

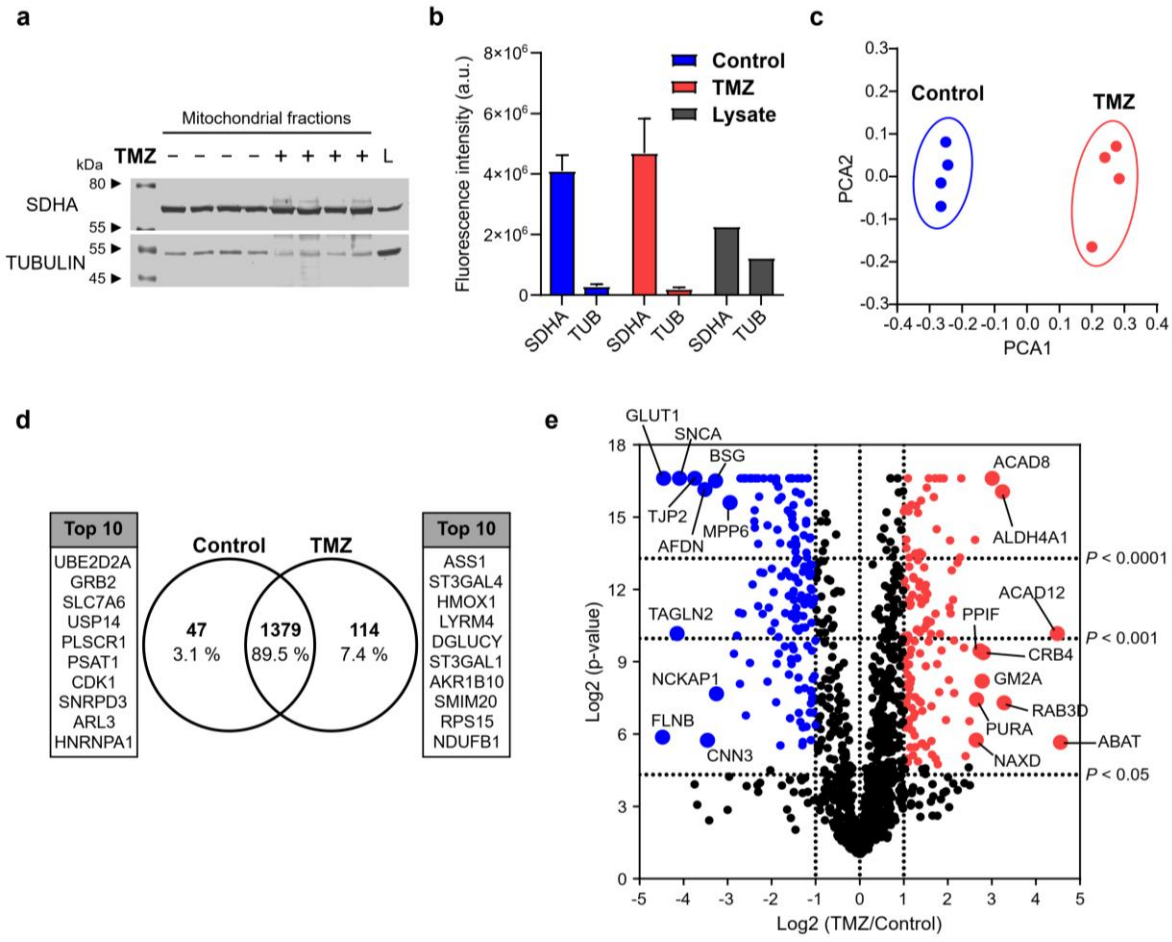


Figure 2. Shotgun proteomic analysis of mitochondria-enriched fractions from senescent melanoma B16-F1 cells. a Western blot analysis of mitochondria-enriched fractions using antibodies against SDHA and tubulin, as mitochondrial and cytosolic markers, respectively. The figure shows four replicates per condition. L denotes total cell lysate. **b** Signal of each band in (a) was quantified using the LI-COR Odyssey imaging system. Data are shown as the mean ± S.D. (n = 4). **c** Principal component analysis of proteins detected in the different mitochondria-enriched samples by mass spectrometry-based shotgun proteomics. **d** Venn diagram showing proteins identified exclusively in control cells, exclusively in TMZ-treated cells, or in both conditions. Tables show the top 10 proteins detected in each condition. **e** Volcano plot of proteins identified in mitochondria-enriched fractions from control and TMZ-treated cells in at least six replicates. Each dot represents one protein, plotted by fold change [Log2(TMZ/control)] and statistical significance [−Log2(BH-adjusted P-value)]. Larger dots indicate the ten proteins with the highest TMZ/control ratio (red) and the ten proteins with the lowest TMZ/control ratio (blue).

Functional enrichment analysis reveals extensive mitochondrial metabolic and structural remodeling in senescent cells

To explore the biological processes associated with the proteomic changes observed between conditions, we performed gene set enrichment analysis (GSEA) using Gene Ontology (GO) Biological Process gene sets. Among the pathways most heavily enriched were amino acid and lipid catabolic routes, the tricarboxylic acid (TCA) cycle, the aerobic electron transport chain, and oxidative phosphorylation (Fig. 3a, Data_file S5), prompting us to identify the proteins involved in these pathways that were higher in the mitochondria of senescent than control cells.

Enzymes involved in fatty acid import into mitochondria (CPT1, CPT2, CRAT) and the β-oxidation pathway (such as ACADVL, ACOT13, ACOT9, ACADSB, HADA, HADB, ETFDH) were significantly increased in senescent cells compared with non-senescent cells (Fig. 3b). Additionally, we present enzymes involved in amino acid and amino acid derivative catabolism, which were significantly increased in senescent cells compared with controls. These include enzymes involved in the degradation of branched-chain amino acids: Leucine and isoleucine to acetyl-CoA (ALDH6, IVD, ACADSB, HSD17B10, DLD) or glutamate (BCAT2) (i) and valine and isoleucine to succinyl-CoA (ACAD8, HIBCH, HIBADH, MMUT) (ii). Enzymes that participate in the conversion of proline to glutamate (ALDH4A1, PRODH), glutamine to glutamate (GLS), and glutamate to α-ketoglutarate (GLUD1) are also shown (Fig. 3b). Interestingly, we also observed a relevant increase in ABAT in senescent cells (fold change TMZ/CTRL = 23.57, *P*-value = 0.02). This enzyme participates in the transamination of GABA to succinic semialdehyde, which in turn is oxidized by NAD^+ to succinate (Fig. 3b)[32]. These catabolic routes converge on acetyl-CoA or TCA cycle intermediates (α-ketoglutarate, succinyl-CoA, and succinate). Accordingly, several TCA cycle enzyme subunits were higher in senescent than in non-senescent melanoma cells (ACO2, IDH3A, IDH3B, IDH3G, DSLT, OGDH, OOGDHL, SUCLA2, SUCLG1, SUCLG2, SDHA, SDHB, MDH2). Higher levels of subunits of the pyruvate dehydrogenase complex (PDHA1, PDHX) were also observed in senescent cells with respect to non-senescent cells (Fig. 3b).

In line with the higher mitochondrial respiration rates observed in senescent cells[12,14] , with respect to control cells, we also observed an increase in several subunits and accessory assembly proteins of electron transport chain complexes I (NDUFA5, NDUFA7, NDUFA12, NDUFB1, NDUFB 4,

NDUFB6, NDUFV3, ACAD9), IV (COA3, COX5B, COX6B1, COX7A21) and ATP synthase (ATP5F1D, ATP5F1E), as well as in enzymes of the ubiquinone (coenzyme Q10) synthesis pathway (COQ6, COQ9) (Fig. 3b). Moreover, an increase in mitochondrial inner membrane translocase subunit Tim8 (TIMM8a1) was also observed in senescent cells. This translocase is involved in the import and insertion of hydrophobic membrane proteins from the cytoplasm into the mitochondrial inner membrane[33].

Higher metabolic rates were accompanied by increased levels of several metabolite transporters located in the mitochondrial inner membrane. These included proteins involved in the transport of serine (SFXN3), citrate (SFXN5), and flavin adenine dinucleotide (FAD) (SLC25A32) (Fig. 3b).

Interestingly, mitochondrial fusion proteins mitofusin 1 (MFN1) and mitofusin 2 (MFN2) were only found in mitochondrial fractions of TMZ-treated cells (Data_file S3). These results are in agreement with the MFN-dependent increase in mitochondrial length in TMZ-induced senescent cells, previously reported by our group[14,34]. Senescence induction was also accompanied by an increase in MICOS complex subunits (MIC13, MIC19, MIC26, and MIC60) (Data_file S4). This complex has a primary role in maintaining the architecture of mitochondrial and cristae junctions and also participates in the inner and outer mitochondrial membrane contact sites[35].

In line with these proteomics findings, NMR-based analysis of intracellular metabolites revealed significant differences between control and senescent cells (Table 1, Fig. S2). Consistent with the observed increase in catabolic enzymes, senescent cells showed decreased levels of the branched-chain amino acids isoleucine, valine, and leucine. Senescent cells also showed reduced levels of other amino acids, including alanine, aspartate, and phenylalanine. In contrast, intracellular glutamine levels were increased (Table 1), which may reflect altered glutamine uptake and/or metabolism, as increased glutamine consumption has been reported in other senescent cell models[36]. Together, these observations support the idea that senescent melanoma cells reprogram amino acid catabolism and may increasingly rely on amino acids as alternative carbon and energy sources to sustain mitochondrial function.

Senescent cells also showed lower levels of the TCA cycle intermediates succinate and fumarate, along with reduced intracellular lactate levels (Table 1), further supporting broad remodeling of central carbon metabolism. Additionally, senescent cells presented higher intracellular levels of the antioxidant tripeptide glutathione (GSH, L-γ-glutamyl-L-cysteinyl-glycine) (Table 1) and the

mitochondrial GSH transporter glutathione (SLC25A40) (Fig. 3b), in agreement with reports of alterations in redox homeostasis in senescence[37–39].

Together, bioenergetic, proteomic, and metabolomic assays indicate that TMZ-induced senescent melanoma cells undergo profound metabolic remodeling. In addition to glucose and fatty acid oxidation, which have been previously identified as important pathways supporting energy production in therapy-induced senescence[14] and oncogene-induced senescence[12,21], our results point to amino acids and their derivatives as additional potential carbon and energy sources. These findings suggest that senescent melanoma cells gain metabolic flexibility, enabling them to use multiple substrates to sustain mitochondrial function and meet energy demands.

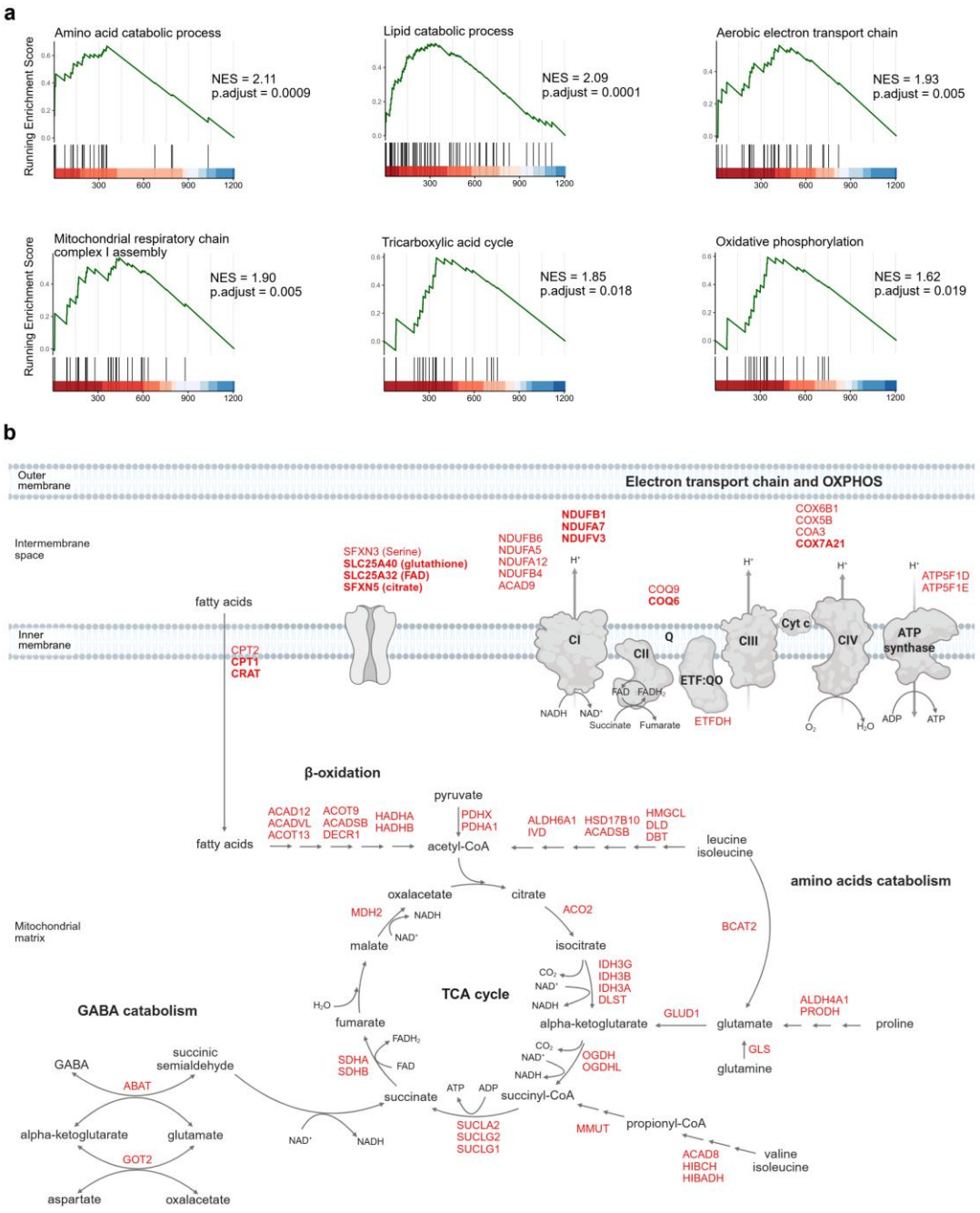


Figure 3. Gene set enrichment analyses and analysis of proteins found exclusively or upregulated in mitochondria-enriched fractions obtained from senescent cells. a Gene set enrichment analyses (GSEA) are shown with their respective Normalized enrichment score (NES) and adjusted P-value (p.adjust). We used the Gene Ontology Biological Process database to analyze mitochondrial proteins between conditions. The x-axis represents the ranked list of all proteins and the y-axis shows the Enrichment Score. A complete list of the GSEA results is provided in Data_file S5. **b** Graphical representation of the proteins found exclusively (bold red) and proteins increased more than 2-fold (red) and with a P-value ≤ 0.05 involved in catabolic pathways, the TCA cycle, ETC, oxidative phosphorylation, and metabolite transport. Complete lists of proteins significantly increased in senescent versus non-senescent cells are shown in Data_files S3 and S4. The figure was created in https://BioRender.com.

Table 1. Intracellular metabolite analysis of B16-F1 cells. Fold change (TMZ/Control) of intracellular metabolites determined by NMR. Data are represented as mean ± S.D. (n = 5), and t-tests were used to determine p-values.

Metabolic pathway	Metabolite	Fold change (TMZ/Control)	P-value
Amino acids metabolism	**Isoleucine**	**-1.15**	**0.00005**
	Valine	**-1.18**	**0.00002**
	Leucine	**-1.08**	**0.0100**
	Alanine	**-1.70**	**4.66E-6**
	Glutamate	-1.06	0.069
	Glutamine	**1.75**	**2.22E-6**
	Aspartate	**-1.14**	**0.00047**
	Glycine	**-1.16**	**0.00003**
	Threonine	**-1.33**	**0.00009**
	Tyrosine	1.00	0.92
	Phenylalanine	**-1.19**	**0.00033**
Glutathione/Redox metabolism	**Glutathione**	**1.20**	**0.00066**
	Pyro-glutamate	**-1.19**	**0.00061**
Creatine metabolism	Creatine	1.05	0.19
	Creatinine	**1.22**	**0.00027**
Membrane metabolism	**Myo-Inositol**	**3.01**	**5.02E-8**
	Taurine	**1.46**	**3.27E-7**
Glycolysis	**Lactate**	**-2.24**	**7.82E-7**
TCA cycle	**Succinate**	**-1.49**	**0.00011**
	Malate	-1.09	0.48
	Fumarate	**-2.28**	**0.00001**
Choline metabolism/phospholipid metabolism	**Phosphocholine**	**1.68**	**9.53E-6**
Small organic acids / one-carbon-related metabolites	Formate	-1.08	0.68
	Acetate	-1.21	0.082
	Beta-alanine	-1.00	0.92
Carbohydrate metabolism	Xylose	-1.08	0.69
Nucleotide-sugar metabolism	UDP-GalNAc	-1.16	0.11
	UDP-Glucose	-1.01	0.81
	UDP-Galactose	1.07	0.76
Nucleotide/energy and redox metabolism	**IMP**	**-2.05**	**0.02**
	GTP	-1.32	0.25
	ADP	-1.02	0.76
	ADP/AMP	-1.19	0.053
	NAD+	**-1.23**	**0.0031**
Other/exogenous or fermentation-related	**Ethanol**	**-2.88**	**0.032**

Therapy-induced senescence increases ABAT levels and expression in melanoma cells

Among the proteins identified, ABAT stood out as one of the most strongly upregulated proteins in senescent cells. Its marked increase (more than 20-fold in senescent cells), together with its potential relevance to the metabolic reprogramming associated with senescence, prompted us to investigate its role further. This enzyme participates in the degradation of GABA, a signaling metabolite that regulates tumor development and immunity and can be metabolized in the TCA cycle (Fig. 3b)[40–43]. First, we confirmed increased ABAT in TMZ-exposed melanoma cells by Western blot (Fig. 4a and 4b). Additionally, RT-qPCR showed increased *Abat* mRNA levels in TMZ-treated versus control cells, suggesting transcriptional upregulation of the enzyme in senescent cells (Fig. 4c).

To further investigate the role of this protein in senescent cells, we generated a knockout (KO) B16-F1 cell line using the CRISPR/Cas9 system with the lentiCRISPR-V2 vector, which was used in the empty form as a control (Fig. 4d). Gene editing was assessed by Sanger sequencing and analyzed using Synthego's Inference of CRISPR Edits (ICE) tool. Two clones showed substantial editing, with KO-scores of 94% for KO #1 and 63% for KO #2, indicating that a high proportion of the inferred edits were predicted to disrupt gene function. ICE analysis identified predominantly 1-bp insertions and deletions in both clones. In KO #1, the major inferred alterations were a 1-bp deletion (46%) and a 1-bp insertion (44%), whereas KO #2 showed a 1-bp insertion (32%), a 1-bp deletion (30%), and a 3-bp deletion (28%). Both analyses had a goodness-of-fit (R^2) of 0.94 (Data_file S6).

After TMZ treatment, both Control and *Abat* KO cells adopted characteristic morphological changes of senescent cells (Fig. 4e), suggesting that Abat KO does not affect TMZ-induced senescence. However, *Abat* KO reduced the percentage of SA-beta-gal-positive cells after TMZ exposure (Fig. 4e). In TMZ-treated cells, *Abat* KO further impaired mitochondrial function, as evidenced by a significant decrease in maximal oxygen consumption rate, spare respiratory capacity, and respiratory control ratio compared with senescent control cells (Fig. 4f, Table 2). Together, these results support a role for ABAT in sustaining mitochondrial electron transport chain activity and the ability of the cell to respond to energy demands[44], particularly in the context of therapy-induced senescence. We next evaluated cell viability after 24 h of incubation in media with different nutrient availability: complete medium (i), serum-free medium supplemented with

glucose, glutamine and pyruvate (ii), or basal DMEM containing only the amino acids present in the medium formulation (iii). TMZ-induced senescent cells maintained similar viability across all media tested (Fig. 4g). In contrast, non-senescent cells showed reduced viability upon serum withdrawal, which was further decreased under more restrictive nutrient conditions (Fig. 4g). Interestingly, *Abat* KO did not modify the sensitivity to FBS removal or nutrient deprivation in non-senescent cells (Fig. 4h). However, in TMZ-induced senescent cells, *Abat* KO markedly reduced cell viability upon serum withdrawal and under nutrient-deprived conditions (Fig. 4h). We confirmed these observations in independent experiments performed with another *Abat* KO clone (*Abat* KO #2) (Fig. S1c-f). These results suggest that ABAT contributes to senescent melanoma cells' ability to tolerate nutrient deprivation, supporting the idea that ABAT-dependent metabolism participates in the adaptive bioenergetic state associated with therapy-induced senescence.

Table 2. Mitochondrial respiratory indices. Coupling efficiency, spare respiratory capacity, and respiratory control ratio calculated from OCR measurements in Fig. 4f. Results are the mean ± S.D. Statistical significance of the main effects of TMZ treatment, *Abat* KO, and their interaction were determined by two-way ANOVA and Tukey post hoc for multiple comparisons. Groups with different letters are significantly different ($P < 0.05$). Main effects of TMZ treatment, *Abat* KO, and their interaction, respectively, for: Coupling efficiency ($P < 0.0001$, $P < 0.0001$, $P < 0.0001$), Spare respiratory capacity ($P < 0.0001$, $P < 0.0001$, $P < 0.0001$), Respiratory control ratio ($P < 0.0001$, $P < 0.05$, $P < 0.0001$).

Respiratory ratios	Control - DMSO	*Abat* KO - DMSO	Control - TMZ	*Abat* KO - TMZ
Coupling efficiency	0.56 ± 0.01^{c}	0.66 ± 0.001^{b}	0.75 ± 0.03^{a}	0.76 ± 0.01^{a}
Spare respiratory capacity	1.7 ± 0.10^{c}	1.7 ± 0.11^{c}	2.7 ± 0.8^{a}	2.0 ± 0.13^{b}
Respiratory control ratio	3.8 ± 0.3^{c}	5.2 ± 0.5^{c}	11.2 ± 1.4^{a}	8.1 ± 0.4^{b}

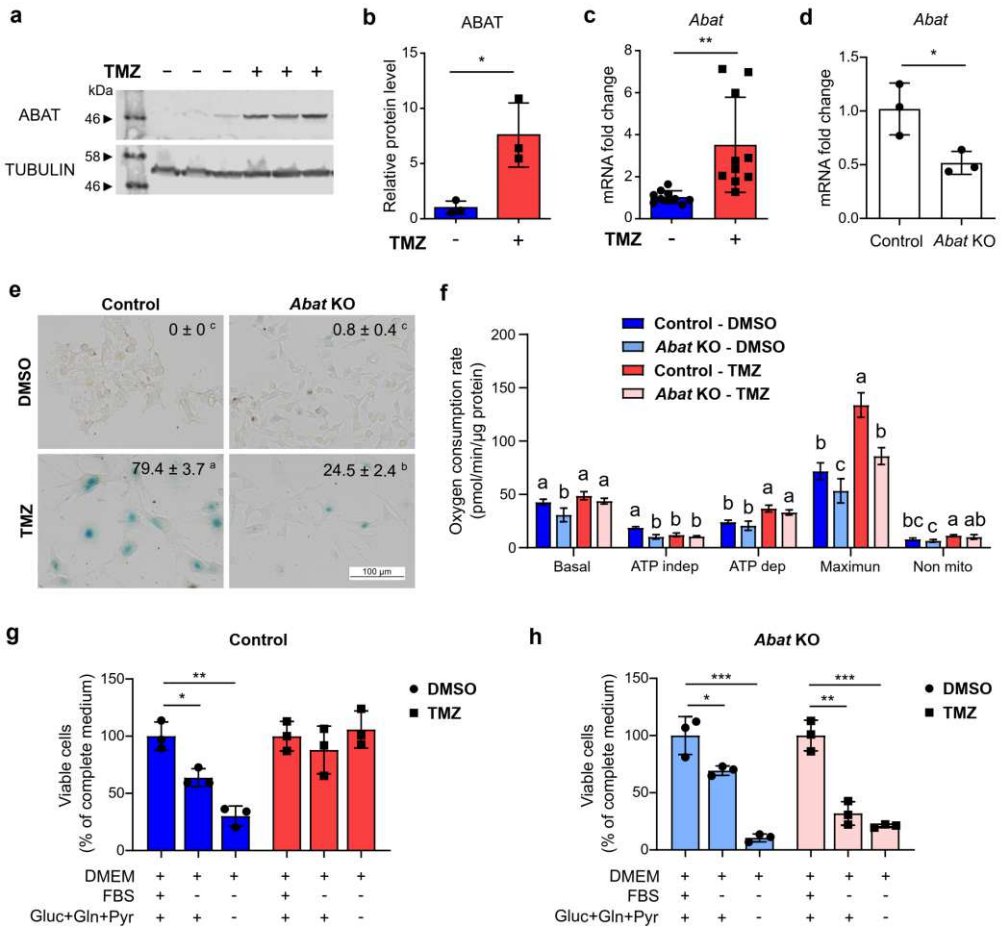


Figure 4. ABAT increased expression sustains mitochondrial respiration and cell viability in therapy-induced senescence in B16-F1 melanoma cells. (**a-c**) B16-F1 cells were exposed to DMSO or TMZ as described in Figure 1. **a** Western blot of cell lysates with antibodies for ABAT and tubulin. **b** ABAT levels were quantified from (a) and normalized using tubulin as a loading control (n = 3). **c** RT-qPCR for *Abat* expression. Results are expressed relative to the control condition (n = 10). (**d-h**) *Abat* expression was knocked out with the CRISPR/Cas9 system; an empty CRISPR-V2 vector was used as a Control. **d** RT-qPCR for *Abat* expression. Results are expressed relative to the Control condition (n = 3). **e** Representative images of the SA-β-gal activity assay. The percentage of SA-β-gal-positive cells after TMZ treatment is shown for each condition (n = 4). **f** Respiratory parameters obtained from oxygen consumption rate (OCR) measurements before and following the sequential addition of 1 µM oligomycin, FCCP (two 1 µM additions), and 1.5 µM antimycin A/1.5 µM rotenone (n = 5). **g** and **h** After 24 hours of incubation in the different media, we counted viable cells using trypan blue exclusion, and we expressed them as a percentage relative to cells cultured in complete medium (DMEM supplemented with glucose, glutamine, pyruvate, and FBS), which was set to 100%. Results are the mean ± S.D. In **b-d**, t-tests were performed. In **e** and **f**, statistical differences were determined by two-way ANOVA and Tukey post hoc for multiple comparisons. Groups with different letters are significantly different ($P < 0.05$). Main effects of TMZ treatment, *Abat* KO, and their interaction, respectively, for: SA-β-gal ($P < 0.0001$, $P < 0.0001$, $P < 0.0001$); Basal OCR ($P < 0.001$, $P < 0.001$, $P = 0.09$); ATP indep. ($P < 0.001$, $P < 0.0001$, $P < 0.0001$); ATP dep. ($P < 0.0001$, $P < 0.05$, $P = 0.94$); Maximum OCR ($P < 0.0001$, $P < 0.0001$, $P < 0.05$); Non mito. $P < 0.0001$, $P = 0.06$, $P = 0.84$). In **g** and **h**, we determined statistical differences by one-way ANOVA and Dunnett's post hoc for multiple comparisons. * $P < 0.05$, ** $P < 0.001$, *** $P < 0.0001$.

Radiotherapy-induced senescence increases mitochondrial mass and *Abat* expression in melanoma cells

To extend our observations to another therapy-induced senescence model, we exposed melanoma cells to the alpha-particle-emitting radioisotope Radium-223 dichloride (^{223}Ra). Four days after ^{223}Ra exposure, we observed an increase in SA-β-gal activity-positive cells (Fig. 5a), in *Cdkn1A* (p21) and SASP components *Il6*, *Ccl2,* and *Ccl5* expression (Fig. 5b), along with morphological changes such as increased cell granularity and size (Fig. 5c). These results indicate that melanoma cells acquire a senescent phenotype after ^{223}Ra exposure. In these radiation-induced senescent melanoma cells, we also observed an increase in mitochondrial respiratory parameters (Fig. 5d, Supplementary Table 1), mitochondrial mass (Fig. 5e), and mtDNA/nDNA ratio (Fig. 5f). Again, the fold increase in maximum respiration rate in senescent versus non-senescent cells exceeded the increase in mtDNA/nDNA levels. Finally, *Abat* expression was higher in ^{223}Ra-induced senescent cells relative to control cells (Fig. 5g).

Together, these results suggest that therapy-induced senescence in melanoma cells is accompanied by increases in mitochondrial mass and proteins, such as ABAT, as well as mitochondrial bioenergetics, regardless of the senescence-inducing stimulus.

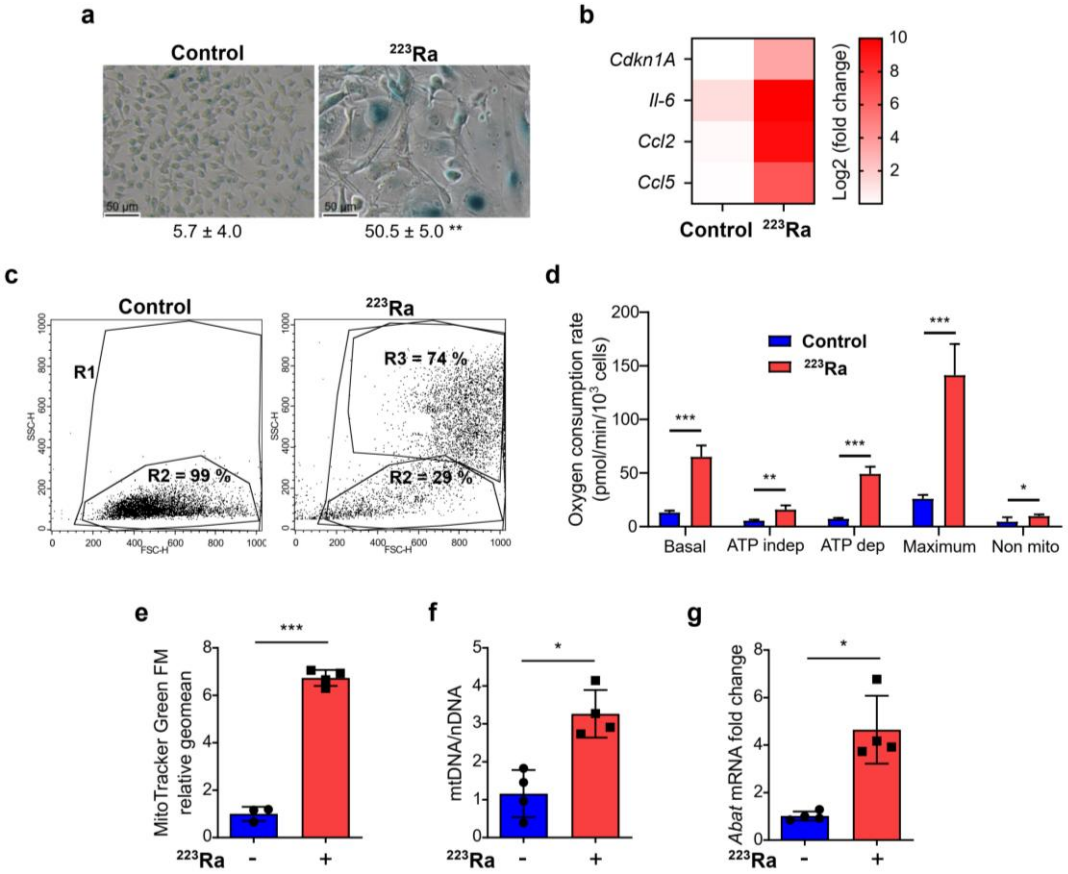


Figure 5. Mitochondrial mass and bioenergetics increase in ^{223}Ra- induced senescence in melanoma cells. B16-F1 cells were exposed to ^{223}Ra (18 kBq) for 48 hours and assessed for four days after treatment. **a** Representative image sof the SA-β-gal activity assay. The percentage of SA-β-gal-positive cells after TMZ treatment is shown for each condition (n = 3). **b** RT-qPCR was performed to analyze *Cdkn1A* (p21*)*, *Il6*, *Ccl2,* and *Ccl5* expression (n = 4); t-tests showed significant differences ($P < 0.05$) in all the assays. **c** Representative dot plot showing cell size (FSC-H) and cell granularity (SSC-H) assessed by flow cytometry. Percentages of cells in R2 and R3 are shown (n = 3-4). **d** Respiratory parameters obtained from oxygen consumption rate (OCR) measurements before and following the sequential addition of 1 µM oligomycin, FCCP (two 1 µM additions), and 1.5 µM antimycin A (n = 6). **e** Cells were stained with MitoTracker Green FM and analyzed by flow cytometry. Relative geometrical mean fluorescence intensity is shown (n = 3-4). **f** mtDNA/nDNA ratio was assessed by qPCR (n=4). **g** RT-qPCR was performed for *Abat* expression. Results are expressed relative to the control condition (n = 4). Results are the mean ± S.D. T-tests were performed. * $P < 0.05$, ** $P < 0.001$, *** $P < 0.0001$.

Therapy increases *Abat* expression and mitochondrial mass in a mouse melanoma model

To translate these observations to an *in vivo* melanoma model, we generated tumors in C57BL/6 mice by inoculating B16-F1 cells into their right flank. When the tumors were palpable, the mice were administered PBS (control) or the chemotherapeutic dacarbazine (DTIC), a temozolomide analog that methylates DNA after being activated in the liver[45]. As expected, DTIC treatment increased animal survival (Fig. 6a, P = 0.0003, Log-rank test) and decreased tumor volume compared with vehicle-treated animals (Fig. 6b and 6c).

Four days after treatment, animals were sacrificed and tumors analyzed. An increase in SA-β-gal staining and size was observed in tumor cells from DTIC-treated mice, compared to the control (Fig. 6d). In addition, higher *Cdkn1a* (p21) expression was detected (Fig. 6e), confirming senescence induction in the tumors as previously reported[34]. Interestingly, *Abat* expression was fourfold higher in tumors from DTIC-treated animals than in controls (Fig. 6f).

To assess mitochondrial mass in tumor cells, we generated B16-F1 cells with a mitochondrial green fluorescent protein (mEGFP) (Fig. 6g and Fig. S3a). mEGFP did not interfere with cell growth or senescence induction by a methylating agent (TMZ) (Fig. S3b and S3c). Mitochondrial mass and bioenergetics in mEGFP B16-F1 cells were also similar to those in B16-F1 cells (Fig. S3d- f), and mEGFP expression did not affect tumor development in mice (Fig. S3g).

We inoculated B16-F1 or B16-F1-mEGFP cells into mice and treated them with DTIC or PBS (control). We excised and disaggregated tumors, and assessed changes in cell size (FSC) and mEGFP fluorescence (FL1) by flow cytometry (Fig. 6h and 6i). Melanoma cells were identified by a high fluorescent signal (R2: $FL1^{high}$), which was present in tumors generated with mEGFP B16-F1 cells (Fig. 6i), but not in those generated with B16-F1 cells (Fig. 6h). Approximately 20-30% of the tumor cells were found in the R2 region, corresponding to mEGFP B16-F1 cells, and no differences were found between animals treated with DTIC or PBS (Fig. 6j). The other cells in the tumor could be immune cells[34] or B16-F1 cells that lost mEGFP expression, among others.

Within the R2 region, we defined a new region containing the cells with a larger size (R3: $FL1^{high}$, FSC^{high}) that we considered to be senescent melanoma cells based on previous studies[14,46]. The cells in R2 with smaller size (R2-R3: $FL1^{high}$, FSC^{low}) were considered non-senescent cells (Fig. 6i). An overall increase in the percentage of fluorescent cells with a larger size (R3: $FL1^{high}$,

444 FSC^{high}) was observed in tumors from DTIC-treated animals, which supported the induction of
445 senescence in tumor cells (Fig. 6i and 6k). Moreover, in treated animals, senescent cells (R3)
446 accounted for 43% of the melanoma cell population (R2) (Fig. 6i and 6l), whereas only 6% of
447 melanoma cells were in the R3 region in control animals (Fig. 6i and 6l).

448 Analysis of the geometrical mean of fluorescence intensity, indicative of mitochondrial content,
449 revealed an increase in fluorescence in the melanoma cell population upon treatment with DTIC,
450 particularly in mEGFP B16-F1 cells with a bigger size (R3 senescent melanoma cells) (Fig. 6m).
451 However, a small but significant increase in mEGFP fluorescence was also observed in non-
452 senescent cells (R2-R3) (Fig. 6m); this increase in mitochondrial mass, along with increased
453 oxidative phosphorylation, could be linked to drug resistance, as reported previously for Mitogen-
454 Activated Protein Kinase (MAPK) inhibitors used to treat melanoma[47–49].

455 In sum, these results suggest that alkylating agents induce senescence in melanoma cells,
456 accompanied by increases in mitochondrial mass and mitochondrial proteins, including ABAT,
457 both *in vitro* and *in vivo*.
458
459
460
461
462
463
464
465
466
467
468
469
470
471
472
473

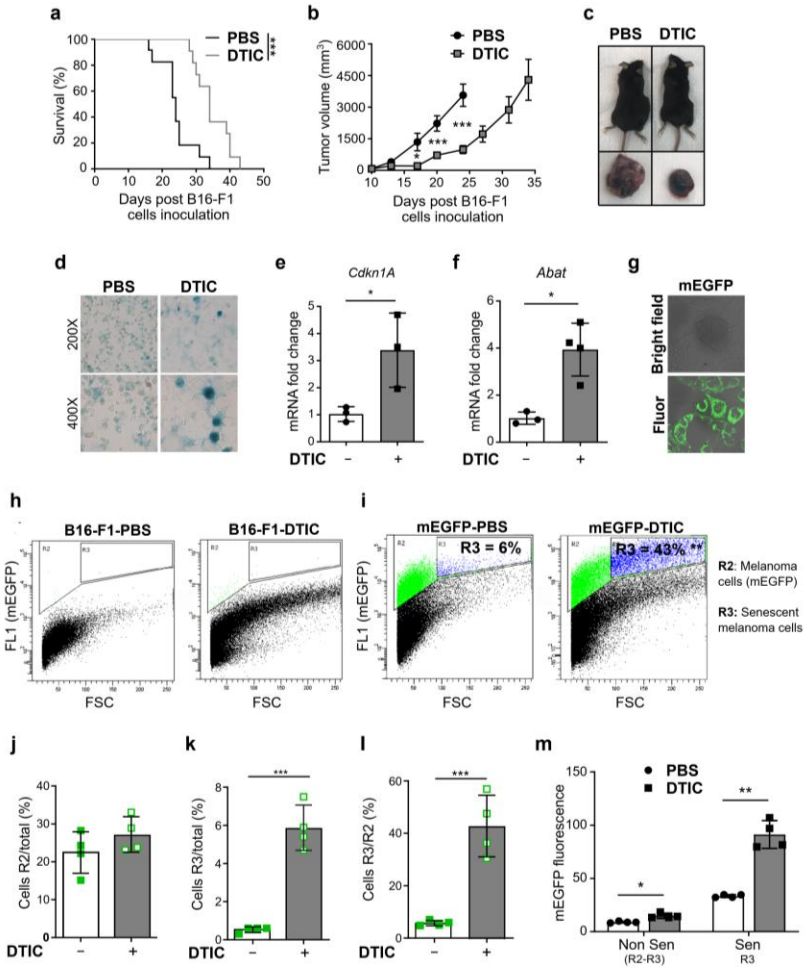


Figure 6. Mitochondrial mass increases in a mouse model of therapy-induced senescence in melanoma. Mice were inoculated subcutaneously with B16-F1 cells and treated with PBS or DTIC as described in the Materials and Methods section. **a** Kaplan-Meier survival curve. The curves show the percentage of surviving mice at the indicated times after inoculation (Log-rank test, *** P = 0.0003). **b** Tumor volume at different times after inoculation (n = 12 mice per group). **c** Representative images of tumors obtained after the animals were sacrificed. **d** Representative images of SA-β-gal staining after tumor disaggregation four days after the last treatment with PBS or DTIC. **e** and **f** RT-qPCR for *Cdkn1a (p21)* (**e**) and *Abat* (**f**) expression in the tumors 8 days after the last DTIC treatment. Results are expressed relative to the control condition (animals treated with PBS) (n = 3-4). **g** Brightfield and fluorescence confocal microscopy images of cells expressing mEGFP. (**h-m**) Mice were inoculated subcutaneously with B16-F1 or B16-F1 mEGFP cells and treated with PBS or DTIC. (**h, i**) Representative dot plots showing cell size (FSC) and cell fluorescence (EGFP-FL1) assessed by flow cytometry after tumor disaggregation, eight days after the last DTIC treatment. R2 shows B16-F1 mEGFP cells ($FL1^{high}$). R3 shows senescent B16-F1 mEGFP cells (FSC^{high} and $FL1^{high}$) (n = 4 mice per group). **j** Percentage of melanoma cells (B16-F1 mEGFP) in the tumor (R2/total). **k** Percentage of senescent melanoma cells (B16-F1 mEGFP) in the tumor (R3/total). **l** Percentage of senescent cells in the melanoma cell population (R2/R3). **m** Geometric Mean of mEGFP fluorescence of non-senescent (R2-R3) and senescent cells (R3) obtained from dot plots in **i** (n = 4 mice per group). Results are the mean ± S.D. T-tests were performed: * P < 0.05, ** P < 0.001, *** P < 0.0001.

p53 regulation of mitochondrial bioenergetics in therapy-induced senescence

We then explored Abat expression regulation. Using the Ominer tool with ChIP-seq datasets from The Signaling Pathways Project[50], we found evidence that tumor suppressor p53 (p53) could bind to the *Abat* gene promoter region in human osteoblasts (SaOS2), fibroblasts (IMR-90), and epithelial (MCF-7) cells (Data_file_S7). In addition, we analyzed the *Abat* gene in humans and mice using the University of California, Santa Cruz (UCSC) Genome Browser, including the DNA sequence 1.5 kb upstream of the transcription start site (TSS)[51]. Although we did not identify putative p53 binding sites in the promoter region of *Abat* in either humans or mice, several sites were identified within the gene body (Fig. S4a–b). Previous studies have shown that transcriptionally active p53 response elements (p53REs) can be located within intragenic regions, particularly within the first intron, and that p53 binding near the TSS is predominantly associated with transcriptional activation of target genes[52,53]. These findings suggest that the identified sites might contribute to the p53-mediated transcriptional regulation of *Abat*.

p53 plays a central role in the DNA damage response and cellular senescence[54] and has also been shown to regulate cell metabolism and mitochondrial function at different levels[55]. Since *Cdkn1a*, a well-known p53 target gene, increased after TMZ exposure and the p53/p21 pathway mediates cell cycle arrest in TMZ-induced senescent cells[14], we explored whether this transcription factor could regulate *Abat* expression and mitochondrial function in senescence.

Based on these observations, we silenced *p53* expression in B16-F1 melanoma cells using lentiviral particles carrying shRNA targeting *p53* (shRNA p53) or a scrambled sequence (Scr). Only one (shRNA p53) of the three shRNAs tested decreased p53 levels in B16-F1 melanoma cells (about 50%) (Fig. S4c-d, Fig. 7a and 7b) and was used in the following experiments.

In *p53*-silenced cells, TMZ treatment significantly reduced SA-β-gal activity and *Cdkn1a* expression (Fig. 7c and 7d), confirming p53's role in inducing senescence by this methylating agent. Consistent with the gene sequence analysis, silencing *p53* reduced *Abat* mRNA levels (Fig. 7d) in both senescent and non-senescent cells, supporting a role for p53 in regulating *Abat* expression. However, whether this regulation is direct or indirect remains unclear.

Moreover, in cells with reduced *p53*, *Pargc1a* expression decreased in both senescent and control cells (Fig. 7d). *Pargc1a* encodes peroxisome proliferator-activated receptor gamma coactivator 1-

alpha (PGC-1-α), a master regulator of mitochondrial biogenesis. Consequently, reduced p53 levels significantly impaired mitochondrial function, reducing all respiratory parameters in senescent melanoma cells (Fig. 7e, Table 3). Similar results were observed when cells were incubated with Pifithrin-α (PFT-α) (Fig. 7f and 7g, Supplementary Table 3), an inhibitor of p53 transcriptional activity[56].

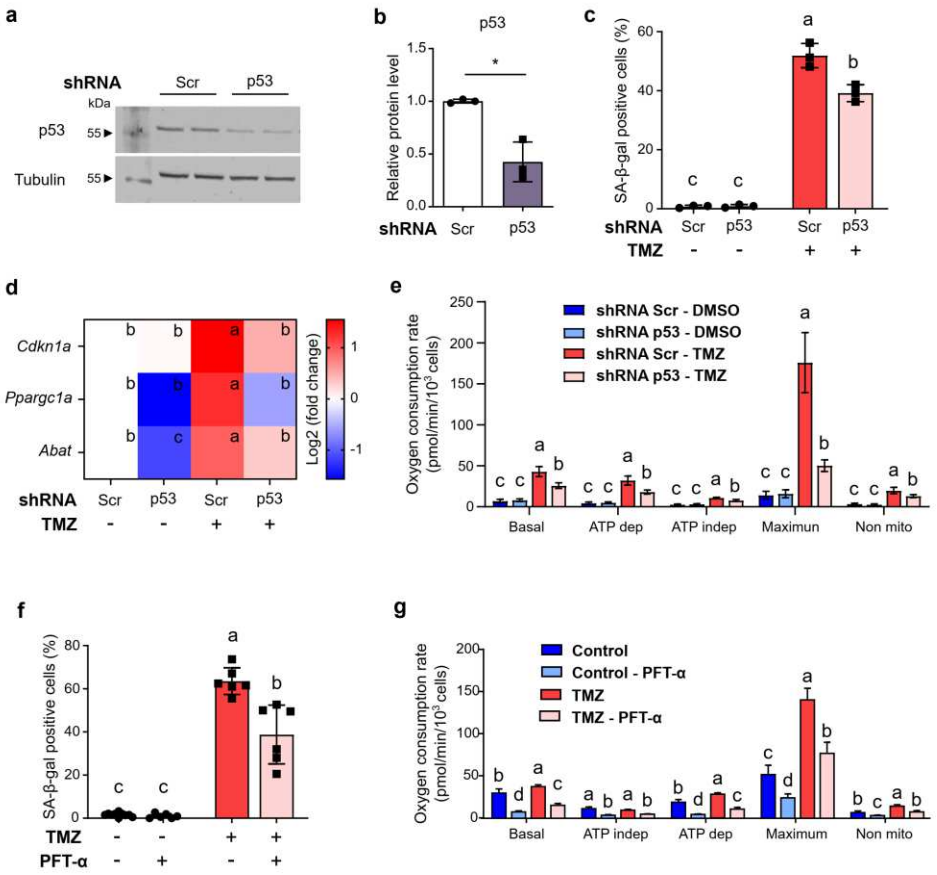


Figure 7. Effects of *p53* silencing on mitochondrial biogenesis and bioenergetics in therapy-induced senescence. (a-e) B16-F1 cells were transduced with lentivirus carrying short hairpin (shRNA) targeting *p53* or scrambled shRNA (Scr), and cells were exposed to DMSO or TMZ as described in Figure 1. **a** Western blots were performed with antibodies for p53 and tubulin. **b** p53 levels were quantified from (**a**) and normalized using tubulin as a loading control (n = 3). **c** Quantification of SA-β-gal activity in the cultures (n = 3). **d** RT-qPCR for *Cdkn1a* (p21), *Ppargc1a* and *Abat* expression. Results are expressed relative to the control condition (shScr - DMSO) (n = 3 – 4). **e** Respiratory parameters obtained from oxygen consumption rate (OCR) measurements before and following the sequential addition of 1 µM oligomycin, FCCP (two 1 µM additions), and 1.5 µM antimycin A/1.5 µM rotenone (n = 5). (**f** and **g**) B16-F1 cells were incubated with 30 µM PFT-α or DMSO 2 hours before TMZ treatment. **f** Quantification of SA-β-gal activity (n = 6). **g** Respiratory parameters obtained as in e (n = 5 wells per group). Results are the mean ± S.D. In **c-g** statistical significance was determined by two-way ANOVA and Tukey post hoc for multiple comparisons. Groups with different letters are significantly different ($P < 0.05$). Main effects of TMZ treatment, *p53* silencing, and their interaction, respectively, for: SA-β-gal ($P < 0.0001$, $P < 0.05$, $P < 0.05$); *Cdkn1a* ($P < 0.05$, $P < 0.05$, $P < 0.05$); *Pgc1α* ($P < 0.0001$, $P < 0.0001$, $P < 0.001$); *Abat* ($P < 0.001$, $P < 0.001$, $P = 0.68$); Basal OCR ($P < 0.0001$, $P < 0.001$, $P < 0.0001$); ATP dep. ($P < 0.0001$, $P < 0.001$, $P < 0.0001$); ATP indep. ($P < 0.0001$, $P < 0.05$, $P < 0.001$); Maximum OCR ($P < 0.0001$, $P < 0.0001$, $P < 0.0001$); Non mito. $P < 0.0001$, $P < 0.05$, $P < 0.05$). Main effects of TMZ treatment, PFT-α treatment, and their interaction, respectively, for: SA-β-gal ($P < 0.0001$, $P < 0.0001$, $P < 0.001$); Basal OCR ($P < 0.0001$, $P < 0.001$, $P = 0.94$); ATP indep. ($P = 0.65$, $P < 0.0001$, $P < 0.05$); ATP dep. ($P < 0.0001$, $P < 0.0001$, $P = 0.12$); Maximum OCR ($P < 0.0001$, $P < 0.0001$, $P < 0.05$); Non mito. $P < 0.0001$, $P < 0.0001$, $P < 0.05$).

We then incubated B16-F1 cells with Nutlin-3, a synthetic inhibitor of the E3 ubiquitin-protein ligase Mdm2 (MDM2), which prevents p53 degradation[57]. Nutlin-3 increased p53 levels and induced *Cdkn1a* expression, increasing p21 protein levels (Fig. 8a-c). *Abat* expression was also higher in Nutlin-3-treated B16-F1 cells than in controls (Fig. 8d), and similar results were observed in human fibroblasts (IMR-90) (Fig. 8e and 8f). Exposure of human fibroblasts to doxorubicin, a chemotherapeutic agent well known to activate the DNA damage response (DDR) and induce senescence[21,58], also increased the expression of both *Cdkn1a* and *Abat* (Fig. 8g-i). These findings strongly suggest that p53 regulates *Abat* expression independently of the inducing stimulus or cell type.

Together, our results indicate that tumor suppressor p53 not only regulates cell cycle arrest in senescence but also regulates mitochondrial metabolism in this setting. In therapy-induced senescence, p53 promotes mitochondrial biogenesis by upregulating *Pargc1a* transcription and catabolic enzymes such as *Abat*, increasing mitochondrial bioenergetics and metabolic flexibility. This allows senescent cells to use different fuels efficiently and favors their survival under energy demand conditions.

Table 3. Mitochondrial respiratory indices. Coupling efficiency, spare respiratory capacity, and respiratory control ratio calculated from OCR measurements in Fig. 7e. Results are the mean ± S.D. Statistical significance of the main effects of TMZ treatment, *p53* silencing, and their interaction were determined by two-way ANOVA and Tukey post hoc for multiple comparisons. Groups with different letters are significantly different ($P < 0.05$). Main effects of TMZ treatment, *p53* silencing, and their interaction, respectively, for: Coupling efficiency ($P < 0.0001$, $P < 0.05$, $P = 0.41$), Spare respiratory capacity ($P < 0.0001$, $P < 0.0001$, $P < 0.0001$), Respiratory control ratio ($P < 0.0001$, $P < 0.0001$, $P < 0.0001$).

Respiratory ratios	ShScr - DMSO	Shp53 - DMSO	ShScr - TMZ	Shp53 - TMZ
Coupling efficiency	0.64 ± 0.01 [b]	0.61 ± 0.03 [b]	0.74 ± 0.02 [a]	0.70 ± 0.02 [b]
Spare respiratory capacity	2.0 ± 0.07 [b]	1.9 ± 0.2 [b]	4.1 ± 0.6 [a]	2.0 ± 0.2 [b]
Respiratory control ratio	5.5 ± 0.09 [b]	5.0 ± 0.5 [b]	16.3 ± 3.2 [a]	6.6 ± 0.8 [b]

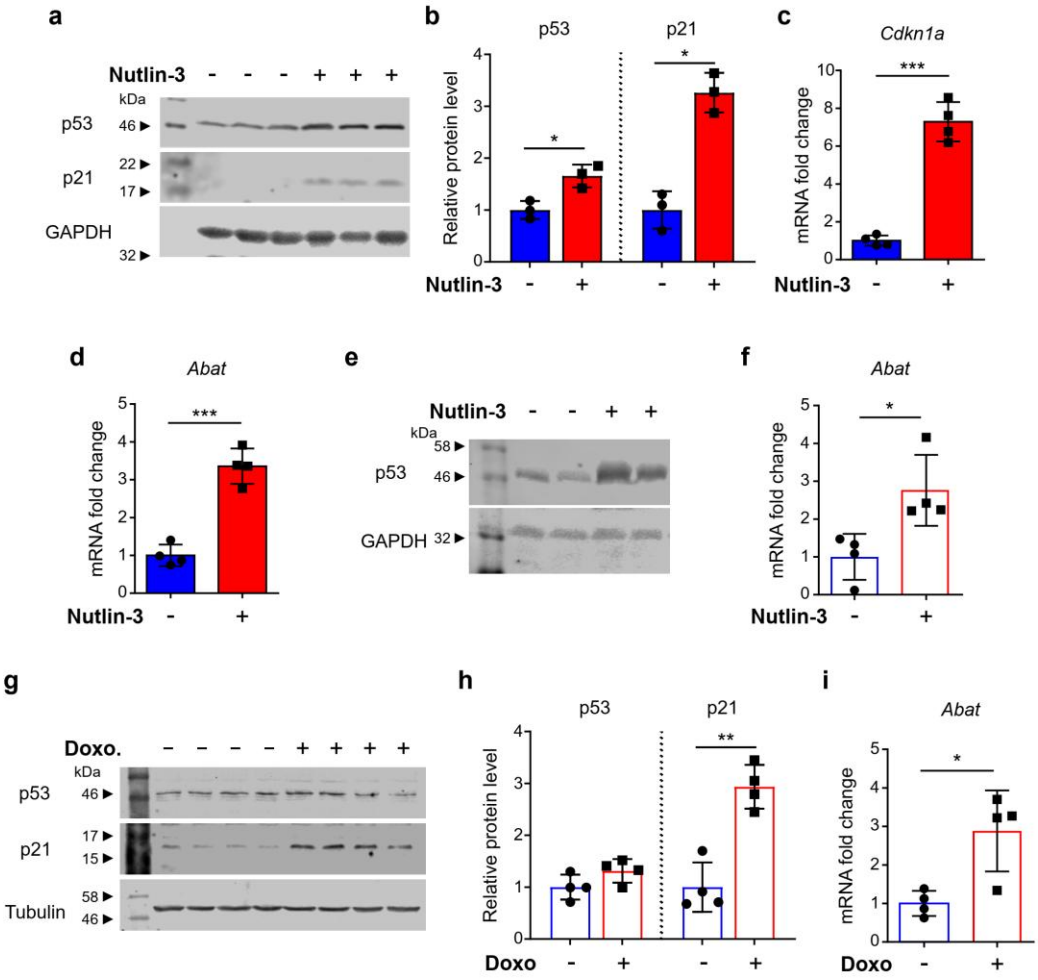


Figure 8. p53 regulates *Abat* expression. (**a-c**) B16-F1 cells were incubated for 24 hours with 10 µM Nutlin-3. **a** Western blots were performed with antibodies for p53, p21, and GAPDH. **b** p53 and p21 levels were quantified from **a**, and normalized using GAPDH as a loading control (n = 3). **c-d** RT-qPCR was performed for *Cdkn1a* (p21) (**c**), and *Abat* (**d**) expression (n = 4). (**e, f**) IMR-90 fibroblasts were incubated for 48 hours with 10 µM Nutlin-3. **e** Western blots were performed with antibodies for p53 and GAPDH. **f** RT-qPCR for *Abat* expression (n = 4). (**g-i**) IMR-90 fibroblasts were incubated for 14 days with 0.2 µM Doxorubicin (Doxo). **g** Western blots were performed with antibodies for p53, p21, and Tubulin. **h** p53 and p21 levels were quantified from **g** and normalized using tubulin as a loading control (n = 4). **i** RT-qPCR for *Abat* expression (n = 4). Results are expressed relative to the control condition (n = 4). Results are the mean ± S.D. T-tests were performed, * $P < 0.05$, ** $P < 0.001$, *** $P < 0.0001$.

Discussion

In the last two decades, the metabolism of senescent cells has been subject to study, and metabolic alterations are now considered characteristic of cellular senescence[59]. Senescence is accompanied by a decrease in fatty acid and nucleotide synthesis and anabolic pathways associated with proliferation[12,58,60]. On the other hand, several studies report an increase in mitochondrial oxidative metabolism, particularly in OIS and TIS, yet metabolic heterogeneity has been observed depending on the senescence-inducing stimuli[21]. OIS is associated with enhanced mitochondrial respiration and fatty acid oxidation, as well as an increase in AMPK and pyruvate dehydrogenase activity[12,16,61]. Similarly, senescent lymphoma cells exposed to chemotherapeutics show elevated glucose uptake and mitochondrial oxidation[11]. In this line, we previously reported that melanoma cells undergoing temozolomide-induced senescence suffer a metabolic reprogramming, shifting from a fermentative to a more oxidative metabolism[14].

In this work, we performed shotgun proteomics to characterize the pathways that support metabolic reprogramming in therapy-induced senescence in melanoma cells. We observed an enrichment of mitochondrial catabolic pathways, particularly lipid and amino acid catabolism, as well as the TCA cycle, electron transport chain, and oxidative phosphorylation in senescent cells. In addition, targeted metabolomic analyses showed decreased levels of several intracellular amino acids, suggesting senescent melanoma cells actively consume these metabolites. These results are consistent with the emerging view that amino acid metabolism is rewired in senescent cells to sustain their increased bioenergetic, biosynthetic, redox, and secretory demands. In particular, recent evidence indicates that branched-chain amino acid metabolism is altered during senescence and can contribute to SASP establishment[62] and that hyperglutaminolysis drives a senescent, pro-aging phenotype[36], both effects through mTORC1 axis activation.

Our results also support an increase in mitochondrial biogenesis, in agreement with previous reports showing elevated mitochondrial mass, mtDNA copy number, PGC1-α, and its downstream target TFAM in TIS, OIS, and DNA damage-induced senescence[17,39,61,63]. Proteomic analysis also revealed changes in several MICOS complex subunits associated with mitochondrial organization and morphology, suggesting that changes in mitochondrial structural organization accompany increased mitochondrial biogenesis.

Among the proteins identified by proteomic analysis in senescent cells, we found ABAT. This enzyme catalyzes the transamination of GABA to succinic aldehyde, forming glutamate and consuming α-ketoglutarate (Fig. 3b). *Abat* expression was augmented in several TIS models, including melanoma cells exposed to TMZ or ^{223}Ra, fibroblasts treated with the topoisomerase inhibitor doxorubicin, and tumors of mice treated with DTIC, suggesting that GABA might serve as an auxiliary energy source in senescent cells.

Abat loss resulted in broad alterations in mitochondrial metabolism, reducing maximum oxygen consumption rate, spare respiratory capacity, and respiratory control ratio in senescent cells. Additionally, *Abat* KO in melanoma and senescent melanoma cells affected cell viability under nutrient-deprived conditions in a medium where amino acids were the only energy source. Thus, the enzyme appears to play a role beyond its canonical catalytic activity.

Our results align with several reports in the literature. In chondrocytes, *Abat* overexpression enhanced mitochondrial respiration and promoted cartilage degradation, while its silencing suppressed respiration, maintained cellular homeostasis, and protected against degeneration[64]. Also, in medulloblastoma, ABAT-dependent GABA metabolism fuels the TCA cycle through succinate, supports oxidative phosphorylation, and promotes survival in the cerebrospinal fluid microenvironment, despite reduced proliferative activity[65]. Additionally, elevated ABAT levels have been observed in T cells, where it metabolizes GABA into succinate, thereby influencing both bioenergetics and cell differentiation[43]. ABAT is also increased in MCF-7 cells overexpressing FOXO1 or WNT1/FGF3 that present a tumor-initiating stem cell phenotype and increased mitochondrial biogenesis[66,67].

Besides its role in GABA catabolism, ABAT could participate in additional mitochondrial pathways relevant to senescence. Besse et al. reported that ABAT forms a mitochondrial complex with the nucleoside diphosphate kinase NME4 and subunits of succinyl-CoA synthetase, including SUCLG1, SUCLG2, and SUCLA2, which is required for mitochondrial deoxynucleotide triphosphate (dNTP) synthesis and maintenance of mtDNA copy number[68]. Interestingly, our proteomic analysis also identified increased levels of NME4 and succinyl-CoA synthetase subunits in senescent melanoma cells (Data_file S3 and Data_file S4). In parallel, we observed increased mtDNA levels, consistent with the higher mitochondrial mass associated with therapy-induced senescence. However, whether ABAT contributes to the increase in mtDNA content observed in

our model remains unknown and should be addressed in future studies. This question is particularly relevant because mtDNA release into the cytosol has been shown to promote the senescence-associated secretory phenotype[19] suggesting that ABAT-associated mitochondrial pathways could potentially influence not only mitochondrial genome maintenance but also inflammatory signaling during senescence.

The increase in *Abat* mRNA levels prompted us to search for transcription factors that could regulate *Abat* expression during senescence. Analysis of the Ominer database suggested p53 as a potential transcriptional regulator, among other candidates. p53 is a central mediator of therapy-induced senescence and has also been implicated in the regulation of cellular metabolism, including glucose metabolism, mitochondrial respiration, and oxidative phosphorylation through targets such as SCO2, a factor that participates in complex IV assembly[55]. In the context of cellular senescence, p53 also contributes to metabolic remodeling. In human fibroblasts, p53-dependent upregulation of glycerol kinase and inhibition of ethanolamine-phosphate cytidylyltransferase (PCYT2) activity promote glycerol-3-phosphate and phosphoethanolamine accumulation, favoring triglyceride storage in lipid droplets and the senescence-associated gene expression program[18]. p53 also represses the expression of the tricarboxylic-acid-cycle-associated malic enzymes ME1 and ME2, reducing NADPH production and altering lipid and glutamine metabolism[69]. In addition, p53 regulates polyamine metabolism and sustains eIF5A hypusination and elevated protein synthesis in senescent cells[70]. More recently, p53 was shown to promote phospholipid headgroup recycling through autophagy and lysosomal catabolism, helping meet the increased demand for membrane phospholipid synthesis during senescence[71]. Together, these studies support a role for p53 in coordinating growth arrest with metabolic adaptations in cellular senescence. In our models, several p53-activating stimuli, including MDM2 inhibition and DNA-damaging agents such as TMZ, DTIC, ^{223}Ra, and doxorubicin, increased *Abat* expression in melanoma cells and human fibroblasts. Conversely, *p53* silencing reduced ABAT levels in TMZ-treated cells, decreased *Pargc1a* expression, and impaired respiration in senescent cells. These findings suggest that p53 helps regulate *Abat* expression and mitochondrial metabolism during therapy-induced senescence. However, further studies are needed to determine whether p53 directly regulates *Abat* transcription.

Overall, our proteomic and metabolomic analyses support a model in which therapy-induced senescent melanoma cells undergo extensive remodeling of mitochondrial metabolic pathways, characterized by increased oxidative phosphorylation, mitochondrial biogenesis, and diversification of catabolic pathways. The enrichment of lipid- and amino acid-catabolic enzymes, along with decreased intracellular amino acid levels, indicates that senescent cells expand the repertoire of substrates they use to meet their energetic demands. Within this metabolic context, ABAT emerges as a mitochondrial enzyme functionally relevant to sustain the enhanced respiratory phenotype and metabolic flexibility of senescent cells. Although ABAT may contribute to GABA catabolism and provide an additional entry point for carbon into the TCA cycle, the effects observed upon *Abat* loss suggest a broader impact on mitochondrial metabolism and cell viability that is not necessarily limited to GABA utilization. Our results further suggest that p53 participates in this adaptive program by coordinating proliferation arrest with mitochondrial remodeling. Thus, ABAT expression appears to be part of the mitochondrial metabolic reprogramming associated with therapy-induced senescence, with potential implications for treatment response in melanoma.

Materials and methods

All reagents were from Sigma unless otherwise specified

Cell culture

Mouse melanoma cells B16-F1 (ATCC, #CRL-6323) and HEK293T (ATCC # CRL-321) were cultured in Dulbecco's modified Eagle's medium (DMEM, Gibco) supplemented with 4.5 g/L glucose, 10% FBS, penicillin 50 U/mL, and streptomycin 50 µg/mL. IMR-90 fibroblasts (CCL-186, ATCC) were cultured in DMEM with 1 g/L glucose supplemented with 10% FBS, penicillin 50 U/mL, and streptomycin 50 µg/mL. Cells were maintained at 37 °C in a CO_2 incubator.

Senescence induction and drug treatments

B16-F1 cells were exposed to two treatments with the methylating agent temozolomide (TMZ) 200 µM for 5 h each, separated by an interval of 24 h as previously described[14]. We established

senescence four days after the second TMZ treatment, and we performed experiments at this time unless otherwise specified.

Alternatively, we incubated B16-F1 cells with 223Ra at 18 kBq/mL for 48 hours and conducted experiments four days later. We employed the calculation model suggested by Roeske and Stinchcomb to determine the absorbed dose of alpha particles, which resulted in 1.3 Gy[72]. We calculated mean cellular microdosimetry assuming cell and nuclear diameters of 10 and 6 µm, respectively.

We exposed IMR-90 cells to doxorubicin (0.2 µM) for 14 days, refreshing the medium every two days. To induce p53 accumulation, B16-F1 and IMR-90 cells were incubated with 10 µM nutlin-3 (Santa Cruz #SC-45061) for 24 or 48 h as specified in each experiment. P53 inhibition was obtained by exposing cells to 30 µM Pifithrin-α (PFT-α, Selleckchem #S2929) 2 h before TMZ treatment and maintained during the experiment.

Dimethyl sulfoxide (DMSO) was the vehicle for TMZ, nutlin-3, PFT-α, and doxorubicin, and the control conditions involved exposing the cells to this solvent.

Subcellular fractionation

We homogenized TMZ-induced senescent and control B16-F1 cells in buffer (10 mM Tris-HCl, 0.25 M sucrose, pH 7.6) using a Potter-Elvehjem homogenizer. Lysates were centrifuged at 1000 g for 10 min at 4 °C to pellet whole cells and nuclei. We obtained mitochondria-enriched fractions by centrifuging the supernatant at 14000 g for 10 min at 4 °C. We washed the pellet twice with homogenization buffer and resuspended it in 10 mM Tris-HCl (pH 7.6) supplemented with SigmaFAST protease inhibitor (#S8830). We evaluated mitochondrial content enrichment by Western blot.

Proteomic analysis by LC-MS/MS

Mitochondria-enriched fractions were run on SDS gels, and equal amounts of protein (10 µg) from each fraction were run on 1 cm-long SDS gels (12% acrylamide). Proteins were fixed with a solution of 50% ethanol and 12% acetic acid and stained with colloidal Coomassie. Protein concentration was determined by comparison with a molecular weight marker (Low Molecular Weight Calibration Kit for SDS Electrophoresis, Amersham). For processing, bands were divided

into smaller portions and destained with 100 mM ammonium bicarbonate, pH 8, 50% acetonitrile (ACN). In-gel cysteine alkylation was performed by incubation with 10 mM dithiothreitol for 1 h at 56ºC followed by incubation with 55 mM iodoacetamide for 45 min at room temperature. We performed in-gel protein digestion with trypsin (Promega) at a 1:50 protein:enzyme ratio in 50 mM ammonium bicarbonate solution (pH 8) at 37ºC overnight, and extracted peptides with 0.1% trifluoroacetic acid in 60% ACN. Samples were dried under vacuum, resuspended in 0.1% formic acid (FA), and cleaned from salts and particles using Ziptip® C18 micro-columns (Millipore).

Tryptic peptides were separated using nano-HPLC (UltiMate 3000, Thermo Scientific) coupled to a Q-Orbitrap hybrid mass spectrometer (Q Exactive Plus, Thermo Scientific). Peptide mixtures were injected into an Acclaim PepMap^{TM} 100 C18 nano-trap column (75 µm x 2 cm x 3 µm, Thermo Scientific) and separated on a pre-analytic column PepMap^{TM} RSLC C18 (75 µm x 50 cm x 2 µm, 100 Å, Thermo Scientific) at a flow rate of 250 nL/min at 40ºC. The column was equilibrated with 1% mobile phase B (A: 0.1% FA; B: 0.1% FA in ACN), followed by an elution gradient as follows: 1–10% B over 30 min; 10–35% B over 120 min; 35–50% B over 30 min; and 50–99% B over 3 min. The mass spectrometer was operated in positive ion mode with a spray voltage of 1.9 kV, a capillary temperature of 250 °C, and an S-lens RF level of 50. We performed mass analysis using a two-step data-dependent acquisition method: MS acquisition over an m/z range of 200–2000, followed by HCD fragmentation of the 12 most intense ions in each segment using stepped normalized collision energies (NCE) of 25, 30, and 35. We acquired both MS and MS/MS spectra at high resolution (70,000 and 17,500 at m/z 200, respectively). We excluded precursor ions with unassigned charge states, charge state 1, or charge states 5 or higher from fragmentation. A dynamic exclusion time of 30 s was applied. Each sample was analyzed in two technical replicates, corresponding to two independent LC–MS injections of the same sample preparation[73].

LC-MS/MS data analysis

Data were analyzed with the software PatternLab for proteomics 4.0 (PatternLab)[74] (http://www.patternlabforproteomics.org). We added the most frequent contaminants in proteomics experiments and the reverse sequence of each protein. We performed the search using the following parameters: mass tolerance from the measured precursor m/z (ppm): 40; enzyme: trypsin; enzyme specificity: fully specific; missed cleavages: 2; variable modifications: methionine

784 oxidation; fixed modifications: carbamidomethylation of cysteine. To achieve a protein-level false
785 discovery rate (FDR) of less than 1%, we filtered peptide spectrum matches using PatternLab's
786 Search Engine Processor (SEPro) module. We accepted only peptides with six or more residues.
787 The mass spectrometry proteomics data have been deposited in the ProteomeXchange Consortium
788 via The PRIDE[75] with the dataset identifier PXD083906.

789 PatternLab's Approximately Area-Proportional Venn Diagram module was used to identify
790 proteins detected exclusively in each biological condition, using an integrated Bayesian model
791 with a *P*-value threshold of ≤ 0.05. The analysis considered proteins present in at least three of
792 four replicates of each biological condition, but absent in all replicates of the other condition. The
793 TFold module applies the Benjamini–Hochberg procedure to correct for multiple *t*-tests and uses
794 a fold-change cutoff that varies with the *P*-value, considering proteins with BH-adjusted *P*-values
795 < 0.05 as differentially abundant[76]. We quantified each protein's abundance from extracted ion
796 chromatograms (XIC). We considered proteins present in six of the eight replicates in both
797 conditions and defined differentially expressed proteins as those meeting the fold-change and P-
798 value criteria. We performed Principal Component Analysis (PCA) using the software's Buzios
799 module.

800 We performed gene set enrichment analysis (GSEA) to identify enriched biological processes
801 using a list of proteins ranked by fold change between conditions. The analysis was conducted
802 using the GSEA software and gene sets from the Biological Process category of the Gene Ontology
803 (GO)[77].

804 **SA-β-galactosidase activity**

805 We determined SA-β-Gal activity using the chromogenic substrate X-gal (Molecular Probes
806 #B1690), as described by Dimri et al., and we calculated the percentage of cells with positive
807 staining by counting at least 100 random cells in five randomly selected microscopic fields[78].

808 **Mitochondrial mass and morphology analyses**

809 Cells were incubated in DMEM without FBS with 300 nM MitoTracker Green FM (Thermo Fisher
810 Scientific) at 37°C for 30 min. We measured the geometric mean fluorescence intensity of the cells
811 to assess mitochondrial mass on a flow cytometer (BD FACSCalibur). Mitochondrial morphology
812 was analyzed by imaging cells with confocal microscopy: Confocal image stacks were acquired

with a Leica TCS-SP5-II confocal microscope (Leica Microsystems) using an HCX PL APO 63x/1.40 oil immersion objective, with 0.2 µm z-stack slice intervals[14].

Western blots

Cells were lysed in lysis buffer (20 mM Tris-HCl pH 7.5, 150 mM NaCl, 0.1% Triton X-100) with protease and phosphatase inhibitors: 1 mM EDTA, 1 mM EGTA, 25 mM sodium pyrophosphate, 25 mM β-glycerophosphate, 1 mM sodium orthovanadate, 1 mM sodium fluoride, 1 mM phenylmethylsulfonyl fluoride, SigmaFAST, and phosphatase inhibitors (Thermo Scientific #A32957). We sonicated samples, centrifuged them at 10000 g for 10 min at 4 °C, and stored them at –80 °C. We used the bicinchoninic acid technique to determine protein concentration.

To resolve the proteins, electrophoresis was performed on SDS-polyacrylamide gels (SDS-PAGE) under reducing conditions and transferred overnight at 4 °C to nitrocellulose membranes (LI-COR Biosciences). The membranes were then blocked for 1 hour at room temperature in Tris-buffered saline (TBS: 50 mM Tris-HCl, pH 7.5, 150 mM NaCl) with 0.1% Tween-20 and 5% nonfat milk. Incubation with the primary incubation with primary antibodies was performed overnight at 4 °C (Supplementary Table 4); for development, secondary antibodies were used: IRDye secondary antibodies: rabbit IRDye® 800 anti-IgG (H+L) (#926-32211, 1:20000) and mouse IRDye® 680 anti-IgG (H+L) (#926-32211, 1:20000) and IRDye® 680 anti-IgG (H+L) (#926-68070, 1:20000) from LI-COR Biosciences. Three washes were performed with TBS containing 0.1% Tween between steps. We used the Odyssey instrument to detect bands on the membranes, and we quantified the images with Image Studio Lite software (LI-COR Biosciences).

RNA extraction and reverse transcription quantitative real-time PCR (RT-qPCR)

We isolated total RNA with TRIzol Reagent (Thermo Scientific #15596026), precipitated it with isopropanol, and quantified it on a Scanning Micro-Volume Spectrophotometer (Janeway 7415). After DNase I treatment (Invitrogen #18068015), we obtained cDNA from 1 µg of total RNA by reverse transcription with random primers (Random hexamer primer, Invitrogen #SO142) and M-MLV reverse transcriptase (Invitrogen #28025-013). We performed real-time quantitative PCR on a Corbett Rotor-Gene 6000 analyzer (Thermo Fisher Scientific) using PowerUp SYBR Green master mix (Applied Biosystems #A25742) and specific primers (Supplementary Table 5). All

PCRs included the amplification of β-actin. For each gene, we calculated the expression relative to actin expression and the control by the $2^{-\Delta\Delta Ct}$ method[79].

DNA extraction and assessment of mtDNA/nDNA ratio

We extracted total DNA using the Quick-DNA Miniprep Plus Kit (Zymo Research, #D4069), quantified DNA by measuring absorbance at 260 nm. We checked sample purity by calculating the A260/A280 ratio on a Scanning Micro-Volume Spectrophotometer (Janeway #7415). We used separate tubes with 15 ng total DNA to amplify mtDNA and nDNA. We performed quantitative RT-PCRs with PowerUp SYBR Green master mix and 0.5 µM of each primer (Supplementary Table 5) and measurements on the Corbett Rotor-Gene 6000 (Thermo Fisher Scientific). The ratio of mtDNA to nDNA was calculated with the $2^{-\Delta\Delta CT}$ method, and the results were expressed relative to the control condition[80].

Oxygen consumption rate measurements

We determined mitochondrial oxygen consumption rate (OCR) using the Seahorse XFe24 extracellular flow analyzer (Agilent). Cells were seeded on polystyrene V7 plates (Agilent), and after 24 hours, the culture medium was replaced with the assay medium: DMEM (Sigma D5030) supplemented with 5 mM glucose, 1 mM sodium pyruvate, 32 mM NaCl, 2 mM glutamine, pH 7.4, and incubated for 1 hour at 37 °C in a CO_2-free incubator. We measured the oxygen consumption rate before and after sequential addition of oligomycin (1 µM), carbonylcyanide-4-(trifluoromethoxy) phenylhydrazone (FCCP) (two 1 µM additions), and antimycin A (1.5 µM) plus rotenone (1.5 µM). At the end of the measurements, we determined cell number with a particle counter (Beckman Coulter) or total protein content by the bicinchoninic acid technique, and we used these values to normalize respiration rates. We determined respiratory parameters as follows: oxygen consumption rate resistant to the addition of antimycin A/rotenone (non-mitochondrial) was subtracted from all measurements to determine oxygen consumption due exclusively to electron transport in the respiratory chain. Respiratory parameters and indices were determined as described previously[14,44]. Briefly, we determined the basal oxygen consumption rate before adding inhibitors and the uncoupler. We used oligomycin, an inhibitor of mitochondrial ATP synthase, to determine oxygen consumption rates independent of and dependent on ATP synthesis in oxidative phosphorylation. With the measurements obtained after the addition of the uncoupler FCCP, we calculated the maximum rate of oxygen consumption[44]. The following respiratory indices were

calculated, considering oxygen consumption rate measurements: coupling efficiency (ATP-dependent OCR/basal OCR), reserve capacity (maximum OCR/basal OCR), and respiratory control ratio (RCR, maximum OCR/oligomycin-resistant OCR)[44].

SCENITH Metabolic analysis

We adapted the protocol of the SCENITH method from Argüello et al. to study melanoma cell energy metabolism by flow cytometry[31]. The method assesses protein synthesis (PS) in the presence of metabolic inhibitors: oligomycin (1 μM), 2-deoxy-D-glucose (100 mM), or a sequential combination of both drugs. The translational initiation inhibitor Harringtonine (H, final concentration 2 μg/mL) was added as a negative control. For the untreated group, an equal volume of DMSO was added to each well as a control (Co). Cells were incubated for 15 min at 37°C, 5% CO_2. After incubation, puromycin (final concentration 10 μg/mL) was added and incubated for 20 min at 37°C, 5% CO_2 to allow incorporation into actively translated proteins. We then performed intracellular staining with a monoclonal anti-Puromycin antibody conjugated to Alexa Fluor 647 to measure protein translation by flow cytometry (Accuri™ C6 Plus Flow Cytometer, BD Biosciences). We used mean fluorescence intensity under different conditions to determine cell dependence on glucose and oxidative phosphorylation for protein synthesis.

NMR sample preparation and data acquisition

For metabolite extraction, we washed control and TMZ-induced senescent B16-F1 cells four times with ice-cold PBS. We then added ice-cold methanol (3.7 mL per 15-cm culture dish), scraped the cells, transferred them to centrifuge tubes, and added methanol (0.3 mL), chloroform (0.4 mL), and ultrapure water (0.5 mL), yielding a final solvent composition of approximately 81.7% methanol, 8.2% chloroform, and 10.1% water (v/v). Samples underwent four 10-s sonication cycles, with 1-min intervals at 4 °C between cycles, then were centrifuged at 15000 × g for 16 min at 4 °C. The aqueous phase was collected and evaporated for 3–4 h at 45 °C using a SpeedVac® SDP1010 concentrator (Thermo Scientific). Dried samples were stored at −80 °C until NMR analysis.

The dry aqueous extracts were mixed with 0.6 mL of a D_2O-based buffer solution, pD 7.4, and transferred to 5 mm NMR tubes (NE HL5 7, New Era Enterprises Inc., Vineland, NJ, USA)[81]. We obtained water-suppressed 1D-NOESY 1H NMR spectra on a Bruker AVANCE III 500 equipped

with a *z*-gradient TXI probe and operating at ^{1}H and ^{13}C frequencies of 500.13 and 125.76 MHz, respectively. We used a spectral width of 10 KHz, a data size of 32 K, and 128 scans with a relaxation delay of 4 s between scans to record each spectrum. When needed, we acquired 1D-TOCSY and HSQC spectra using the spectrometer's default parameters.

NMR data processing

NMR data were processed and analyzed with MNova (version 14.0, MestreLab Research, S.L., Santiago de Compostela, Spain). Free induction decays were zero-filled to 128 K points and apodised with a 0.3 Hz exponential window function before Fourier transformation. All spectra were manually phase- and baseline-corrected, and referenced to the anomeric proton signal of α-glucose (5.22 ppm). Spectra were manually aligned, and the data were normalized to the total spectral area after excluding the residual water resonance region and regions without signals.

Metabolite identification and estimation of relative concentrations

Metabolites were identified by comparison of ^{1}H NMR data against spectral repositories, including the Biological Magnetic Resonance Bank (BMRB)[82], the Human Metabolome Database (HMDB)[83], and Chenomx (version 9, Chenomx, Inc., Edmonton, Canada). We confirmed metabolite identification using 1D TOCSY and HSQC spectra when needed. We estimated metabolite-level variations using relative concentrations. Data are reported as the ratio of the area of an individual metabolite 1H NMR signal to the total spectrum area, which was used for subsequent univariate analysis.

Transduction with lentiviral particles

We purchased plasmids encoding short hairpin RNA (shRNA) targeting different regions of p53 mRNA: TRCN0000012358 (shRNA p53_#3), TRCN0000012359 (shRNA p53_#2), and TRCN00000012360 (shRNA p53) from Dharmacon or Horizon, respectively. The plasmid with a control shRNA scrambled sequence (Addgene #1864), the plasmids pCMV-VSVG (Addgene #8454) and pCMV-dR8.2 dvpr (Addgene #8455) were a gift from Bob Weinberg[84] . HEK293T cells were used to generate lentiviral particles following protocols established by the Broad Institute RNAi Consortium (https://portals.broadinstitute.org/gpp/public/). HEK293T cells were transfected with 1 μg of plasmid pCMV-dR8.2 dvpr, 0.125 μg of plasmid pCMV-VSVG, and 1

µg of the plasmid carrying shRNA in DMEM (without FBS) with Turbofect (Thermo Fisher Scientific). After 24 h, we changed the medium to complete medium. We collected the medium 24 h later, filtered it, centrifuged it, and stored it at -80ºC. Transduction of B16-F1 cells with the lentiviruses was performed overnight in complete medium containing 8 µg/ml hexadimethrine bromide (polybrene). The next day, we replaced the culture medium with complete medium supplemented with 2 µg/ml puromycin to select cells carrying shRNA plasmids. After obtaining a puromycin-resistant culture, we verified silencing by RT-qPCR and/or western blot.

A B16-F1 cell line stably expressing the green fluorescent protein EGFP in the mitochondria (mEGFP) was generated with lentiviral particles carrying the plasmid pLYS1-FLAG-MitoGFP-HA (Addgene plasmid #50057 was a gift from Vamsi Mootha)[85]. We assessed cell population enrichment by sorting based on fluorescence intensity after puromycin selection using a BD FACSAriaTM Fusion cell sorter (BD Biosciences) equipped with a solid-state 488 nm diode laser. For doublet discrimination, we analyzed FSC-A versus FSC-H. We sorted cells using a 70-mm nozzle at 10000 events per second in Purity mode.

Generation of CRISPR/Cas9 Abat-knockout B16-F1 cells

We designed guide RNAs (sgRNAs) for our Abat-editing vector using the CRISPR-based tool CHOPCHOP (https://chopchop.cbu.uib.no/) and purchased them from Macrogen. Lipofectamine™ 3000 (Invitrogen™, L3000001) was used to transfect the lentiCRISPRv2 plasmid (Addgene, #52961) carrying guide RNA (sgRNA: AACGGTGGCTGGAATCATCG) for ABAT (NC_000082.7, Gene ID: 268860) into B16-F1 cells following the manufacturer's protocol. We transfected an empty lentiCRISPRv2 plasmid to generate our control cell line. Transfected cells were grown in complete DMEM containing 2 µg/µL puromycin for 2-3 weeks; cell colonies were then isolated and transferred into fresh growth media for propagation. Potential off-target sites were assessed using CHOPCHOP (Data_file_S6). We confirmed gene editing in the selected clones by Sanger sequencing of PCR-amplified fragments encompassing the predicted editing site using specific primers (Data_file_S6), and we analyzed the resulting chromatograms with Synthego's Inference of CRISPR Edits (ICE) tool (ICE CRISPR Analysis. 2026. EditCo Bio, https://ice.editco.bio/#/).

Cell viability assay

Four days after senescence induction, cells were cultured for 24 hours in DMEM (#5030, Sigma-Aldrich) without supplementation (nutrient-deprived medium); DMEM supplemented with 20 mM glucose, 2 mM glutamine, 1 mM pyruvate (medium); or DMEM supplemented with 20 mM glucose, 2 mM glutamine,1 mM pyruvate, and 10% FBS (complete medium). We assessed cell viability by Trypan Blue exclusion and expressed the number of viable cells in each condition as a percentage relative to viable cells cultured in complete medium (100%).

Murine melanoma model

Female C57BL/6 mice (Dilave, Uruguay), 6–8 weeks old and weighing 19–23 g, were used for *in vivo* experiments. Animals were housed on a 12:12-hour light/dark cycle with controlled temperature (22 ± 2 °C) and humidity (60%), with water and food *ad libitum*. The University's Ethical Committee for Animal Experimentation (CHEA), Uruguay, approved all animal experimentation protocols, which complied with current national laws on Animal Experimentation (protocols 155 and 1793). This study was reported in accordance with ARRIVE guidelines 2.0[86].

The murine melanoma model was established as previously[34,87]. Briefly, we inoculated $2.5x10^5$ melanoma cells (B16-F1 cells or B16-F1 cells expressing mEGFP) subcutaneously in the right flank of C57BL/6 mice, yielding one primary tumor per mouse. When tumors were palpable, approximately 10 days post tumor inoculation (p.t.i.), we treated mice intraperitoneally for three consecutive days with dacarbazine (DTIC) 150 mg/kg/dose or vehicle (PBS). DTIC is a methylating agent, an analog of TMZ, that requires activation in the liver[88]. Mice were weighed every 2-3 days, tumor size was measured with calipers, and volume was calculated as length × width × depth × π/6. Overall survival was assessed based on the day mice died. Mice were sacrificed by cervical dislocation when tumor volume exceeded 4000 mm^3 or earlier if they showed any sign of distress. On the indicated days, we disaggregated tumors and analyzed cells by flow cytometry or cytospin-adhered slides for SA-β-gal staining; alternatively, we extracted tumor RNA and performed RT-qPCR as described above.

Statistical analysis and graphs

All plots and statistical analyses were performed using GraphPad Prism 8.0. Data were analyzed using two-tailed unpaired Student's *t*-tests when comparing two groups, or one- or two-way ANOVA followed by Dunnett's or Tukey's post hoc tests, as appropriate, when comparing more

than two groups. We considered a P-value < 0.05 statistically significant. Data are presented as bar graphs with individual data points in most cases, and values reported in the text are expressed as mean ± S.D. Unless otherwise indicated, n represents the number of independent biological samples, including wells, culture dishes per group or condition. All experiments were performed with $n \geq 3$.

References

1. Mylonas, A. & O'Loghlen, A. Cellular Senescence and Ageing: Mechanisms and Interventions. *Front. Aging* **3**, 866718 (2022).
2. Suryadevara, V. *et al.* SenNet recommendations for detecting senescent cells in different tissues. *Nat. Rev. Mol. Cell Biol.* **25**, 1001–1023 (2024).
3. Collado, M. & Serrano, M. Senescence in tumours: Evidence from mice and humans. *Nat. Rev. Cancer* **10**, 51–57 (2010).
4. Chang, B.-D. B.-D. *et al.* Molecular determinants of terminal growth arrest induced in tumor cells by a chemotherapeutic agent. *Proc. Natl. Acad. Sci.* **99**, 389–394 (2002).
5. Gonzalez, L. C., Ghadaouia, S., Martinez, A. & Rodier, F. Premature aging/senescence in cancer cells facing therapy: good or bad? *Biogerontology* **17**, 71–87 (2016).
6. Ohtani, N. The roles and mechanisms of senescence-associated secretory phenotype (SASP): can it be controlled by senolysis? *Inflamm. Regen.* **42**, 1–8 (2022).
7. Saleh, T., Tyutyunyk-Massey, L. & Gewirtz, D. A. Tumor cell escape from therapy-induced senescence as a model of disease recurrence after dormancy. *Cancer Res.* **79**, 1044–1046 (2019).
8. Demaria, M. *et al.* Cellular senescence promotes adverse effects of chemotherapy and cancer relapse. *Cancer Discov.* **7**, 165–176 (2017).
9. He, Y. *et al.* Cellular senescence and radiation-induced pulmonary fibrosis. *Transl. Res.* **209**, 14–21 (2019).
10. Wang, H. *et al.* Senolytics (DQ) mitigates radiation ulcers by removing senescent cells. *Front. Oncol.* **9**, 1576 (2020).
11. Dörr, J. R. *et al.* Synthetic lethal metabolic targeting of cellular senescence in cancer therapy. *Nature* **501**, 421–425 (2013).

12. Quijano, C. *et al.* Oncogene-induced senescence results in marked metabolic and bioenergetic alterations. *Cell Cycle* **11**, 1383–1392 (2012).
13. Takebayashi, S. *et al.* Retinoblastoma protein promotes oxidative phosphorylation through upregulation of glycolytic genes in oncogene-induced senescent cells. *Aging Cell* **14**, 689–697 (2015).
14. Martínez, J. *et al.* Mitofusins modulate the increase in mitochondrial length, bioenergetics and secretory phenotype in therapy-induced senescent melanoma cells. *Biochem. J.* BCJ20190405 (2019).
15. Nacarelli, T. *et al.* NAD + metabolism governs the proinflammatory senescence-associated secretome. *Nat. Cell Biol.* **21**, 397–407 (2019).
16. Kaplon, J. *et al.* A key role for mitochondrial gatekeeper pyruvate dehydrogenase in oncogene-induced senescence. *Nature* **498**, 109–112 (2013).
17. Correia-Melo, C. *et al.* Mitochondria are required for pro-ageing features of the senescent phenotype. *EMBO J.* **35**, 724–742 (2016).
18. Tighanimine, K. *et al.* A homoeostatic switch causing glycerol-3-phosphate and phosphoethanolamine accumulation triggers senescence by rewiring lipid metabolism. *Nat. Metab.* **6**, 323–342 (2024).
19. Victorelli, S. *et al.* Apoptotic stress causes mtDNA release during senescence and drives the SASP. *Nature* **622**, 627–636 (2023).
20. López-Polo, V. *et al.* Release of mitochondrial dsRNA into the cytosol is a key driver of the inflammatory phenotype of senescent cells. *Nat. Commun.* **15**, 7378 (2024).
21. Marmisolle, I. *et al.* Oncogene-induced senescence mitochondrial metabolism and bioenergetics drive the secretory phenotype: further characterization and comparison with other senescence-inducing stimuli. *Redox Biol.* **82**, 103606 (2025).
22. Martini, H. *et al.* Mitochondrial metabolism and epigenetic crosstalk drive SASP. *Nature* **656**, 980–992 (2026).

23. Saleem, A., Adhihetty, P. J. & Hood, D. A. Role of p53 in mitochondrial biogenesis and apoptosis in skeletal muscle. *Physiol. Genomics* **37**, 58–66 (2008).
24. Lago, C. U., Sung, H. J., Ma, W., Wang, P. & Hwang, P. M. p53, aerobic metabolism, and cancer. *Antioxid. Redox Signal.* **15**, 1739–1748 (2011).
25. Hwang, P. M. *et al.* Ferredoxin reductase affects p53-dependent, 5-fluorouracil–induced apoptosis in colorectal cancer cells. *Nat. Med.* **7**, 1111–1117 (2001).
26. Matoba, S. *et al.* p53 regulates mitochondrial respiration. *Science* **312**, 1650–1653 (2006).
27. Park, J.-Y. *et al.* p53 improves aerobic exercise capacity and augments skeletal muscle mitochondrial DNA content. *Circ. Res.* **105**, 705–712 (2009).
28. Donahue, R. J., Razmara, M., Hoek, J. B. & Knudsen, T. B. Direct influence of the p53 tumor suppressor on mitochondrial biogenesis and function. *FASEB J.* **15**, 635–644 (2001).
29. Park, J., Zhuang, J., Li, J. & Hwang, P. M. p53 as guardian of the mitochondrial genome. *FEBS Lett.* **590**, 924–934 (2016).
30. Saleem, A. & Hood, D. A. Acute exercise induces tumour suppressor protein p53 translocation to the mitochondria and promotes a p53–Tfam–mitochondrial DNA complex in skeletal muscle. *J. Physiol.* **591**, 3625–3636 (2013).
31. Argüello, R. J. *et al.* SCENITH: A Flow Cytometry-Based Method to Functionally Profile Energy Metabolism with Single-Cell Resolution. *Cell Metab.* **32**, 1063-1075.e7 (2020).
32. Osei, Y. D. & Churchich, J. E. Screening and sequence determination of a cDNA encoding the human brain 4-aminobutyrate aminotransferase. *Gene* **155**, 185–187 (1995).
33. Paschen, S. A. *et al.* The role of the TIM8-13 complex in the import of Tim23 into mitochondria. *EMBO J.* **19**, 6392–6400 (2000).
34. Tarallo, D. *et al.* Mitofusin 1 silencing decreases the senescent associated secretory phenotype, promotes immune cell recruitment and delays melanoma tumor growth after chemotherapy. *Sci. Rep.* **14**, 909 (2024).

35. Stephan, T. *et al.* MICOS assembly controls mitochondrial inner membrane remodeling and crista junction redistribution to mediate cristae formation. *EMBO J.* **39**, e104105 (2020).
36. Chen, H. *et al.* Hyperglutaminolysis drives senescence and aging through arginine-mTORC1 axis activation. *Signal Transduct. Target. Ther.* **11**, 64 (2026).
37. Correia-Melo, C., Hewitt, G. & Passos, J. F. Telomeres, oxidative stress and inflammatory factors: partners in cellular senescence? *Longev. Heal.* **3**, 1 (2014).
38. Chacón, E., Grünwaldt, G., Marmisolle, I., Martínez, J. & Quijano, C. Redox metabolism in cell senescence: focusing on contributions from the metabolomic field. *Front. Mol. Biosci.* **12**, 1754469 (2025).
39. Lee, A. C. *et al.* Ras proteins induce senescence by altering the intracellular levels of reactive oxygen species. *J. Biol. Chem.* **274**, 7936–7940 (1999).
40. Zhang, B. *et al.* B cell-derived GABA elicits IL-10+ macrophages to limit anti-tumour immunity. *Nature* **599**, 471–476 (2021).
41. Yang, Y. *et al.* GABAergic signaling as a potential therapeutic target in cancers. *Biomed. Pharmacother. Biomedecine Pharmacother.* **161**, 114410 (2023).
42. Huang, D. *et al.* Cancer-cell-derived GABA promotes β-catenin-mediated tumour growth and immunosuppression. *Nat. Cell Biol.* **24**, 230–241 (2022).
43. Kang, S. *et al.* GAB functions as a bioenergetic and signalling gatekeeper to control T cell inflammation. *Nat. Metab.* **4**, 1322–1335 (2022).
44. Brand, M. D. & Nicholls, D. G. Assessing mitochondrial dysfunction in cells. *Biochem. J.* **435**, 297–312 (2011).
45. Marchesi, F. *et al.* Triazene compounds: mechanism of action and related DNA repair systems. *Pharmacol. Res.* **56**, 275–287 (2007).
46. Gorbunova, V., Seluanov, A. & Pereira-Smith, O. M. Evidence that high telomerase activity may induce a senescent-like growth arrest in human fibroblasts. *J. Biol. Chem.* **278**, 7692–7698 (2003).

47. Corazao-Rozas, P. *et al.* Mitochondrial oxidative phosphorylation controls cancer cell's life and death decisions upon exposure to MAPK inhibitors. *Oncotarget* **7**, 39473–39485 (2016).
48. Prado-Souza, L. F. L. do *et al.* Exploiting Paradoxical Activation of Oncogenic MAPK Signaling by Targeting Mitochondria to Sensitize NRAS Mutant-Melanoma to Vemurafenib. *Int. J. Mol. Sci.* **26**, 2675 (2025).
49. Zhang, G. *et al.* Targeting mitochondrial biogenesis to overcome drug resistance to MAPK inhibitors. *J. Clin. Invest.* **126**, 1834–1856.
50. Ochsner, S. A. *et al.* The Signaling Pathways Project, an integrated 'omics knowledgebase for mammalian cellular signaling pathways. *Sci. Data* **6**, 252 (2019).
51. Kent, W. J. *et al.* The human genome browser at UCSC. *Genome Res.* **12**, 996–1006 (2002).
52. Fischer, M. Census and evaluation of p53 target genes. *Oncogene* **36**, 3943–3956 (2017).
53. Sammons, M. A., Nguyen, T.-A. T., McDade, S. S. & Fischer, M. Tumor suppressor p53: from engaging DNA to target gene regulation. *Nucleic Acids Res.* **48**, 8848–8869 (2020).
54. Muñoz-Espín, D. & Serrano, M. Cellular senescence: from physiology to pathology. *Nat. Rev. Mol. Cell Biol.* **15**, 482–496 (2014).
55. Liu, J., Zhang, C., Hu, W. & Feng, Z. Tumor suppressor p53 and metabolism. *J. Mol. Cell Biol.* **11**, 284–292 (2019).
56. Murphy, P. J. M. *et al.* Pifithrin-alpha inhibits p53 signaling after interaction of the tumor suppressor protein with hsp90 and its nuclear translocation. *J. Biol. Chem.* **279**, 30195–30201 (2004).
57. Karimian, A., Ahmadi, Y. & Yousefi, B. Multiple functions of p21 in cell cycle, apoptosis and transcriptional regulation after DNA damage. *DNA Repair* **42**, 63–71 (2016).
58. Marmisolle, I. *et al.* Reciprocal regulation of acetyl-CoA carboxylase 1 and senescence in human fibroblasts involves oxidant mediated p38 MAPK activation. *Arch. Biochem. Biophys.* **613**, 12–22 (2017).

59. Suryadevara, V. *et al.* SenNet recommendations for detecting senescent cells in different tissues. *Nat. Rev. Mol. Cell Biol.* 1–23 (2024).
60. Aird, K. M. *et al.* Suppression of nucleotide metabolism underlies the establishment and maintenance of oncogene-induced senescence. *Cell Rep.* **3**, 1252–1265 (2013).
61. Moiseeva, O., Bourdeau, V., Roux, A., Deschênes-Simard, X. & Ferbeyre, G. Mitochondrial dysfunction contributes to oncogene-induced senescence. *Mol. Cell. Biol.* **29**, 4495–4507 (2009).
62. Liang, Y. *et al.* Branched-Chain Amino Acid Accumulation Fuels the Senescence-Associated Secretory Phenotype. *Adv. Sci.* **11**, 2303489 (2023).
63. Bartoletti-Stella, A. *et al.* Gamma rays induce a p53-independent mitochondrial biogenesis that is counter-regulated by HIF1α. *Cell Death Dis.* **4**, e663 (2013).
64. Shen, J. *et al.* Inhibition of 4-aminobutyrate aminotransferase protects against injury-induced osteoarthritis in mice. *JCI Insight* **4**, e128568, 128568 (2019).
65. Martirosian, V. *et al.* Medulloblastoma uses GABA transaminase to survive in the cerebrospinal fluid microenvironment and promote leptomeningeal dissemination. *Cell Rep.* **35**, 109302 (2021).
66. Lamb, R. *et al.* Mitochondrial mass, a new metabolic biomarker for stem-like cancer cells: Understanding WNT/FGF-driven anabolic signaling. *Oncotarget* **6**, 30453–30471 (2015).
67. De Luca, A. *et al.* Mitochondrial biogenesis is required for the anchorage-independent survival and propagation of stem-like cancer cells. *Oncotarget* **6**, 14777–14795 (2015).
68. Besse, A. *et al.* The GABA transaminase, ABAT, is essential for mitochondrial nucleoside metabolism. *Cell Metab.* **21**, 417–427 (2015).
69. Jiang, P., Du, W., Mancuso, A., Wellen, K. E. & Yang, X. Reciprocal regulation of p53 and malic enzymes modulates metabolism and senescence. *Nature* **493**, 689–693 (2013).
70. Jiang, X. *et al.* P53-dependent hypusination of eIF5A affects mitochondrial translation and senescence immune surveillance. *Nat. Commun.* **15**, 7458 (2024).

71. Yashinskie, J. J. *et al.* p53 increases phospholipid headgroup scavenging in senescence. *Nat. Cell Biol.* **28**, 296–306 (2026).
72. Roeske, J. C. & Stinhcomb, T. G. Dosimetric framework for therapeutic alpha-particle emitters. *J. Nucl. Med.* **38**, 1923–1929 (1997).
73. Cal, K. *et al.* A nitroalkene derivative of salicylate, SANA, induces creatine-dependent thermogenesis and promotes weight loss. *Nat. Metab.* **7**, 1550–1569 (2025).
74. Carvalho, P. C. *et al.* Integrated analysis of shotgun proteomic data with PatternLab for proteomics 4.0. *Nat. Protoc.* **11**, 102–117 (2016).
75. Perez-Riverol, Y. *et al.* The PRIDE database at 20 years: 2025 update. *Nucleic Acids Res.* **53**, D543–D553 (2025).
76. Carvalho, P. C., Yates, J. R. & Barbosa, V. C. Improving the TFold test for differential shotgun proteomics. *Bioinformatics* **28**, 1652–1654 (2012).
77. Subramanian, A. *et al.* Gene set enrichment analysis: a knowledge-based approach for interpreting genome-wide expression profiles. *Proc. Natl. Acad. Sci. U. S. A.* **102**, 15545–15550 (2005).
78. Dimri, G. P. *et al.* A biomarker that identifies senescent human cells in culture and in aging skin in vivo. *Proc. Natl. Acad. Sci. U. S. A.* **92**, 9363–9367 (1995).
79. Livak, K. J. & Schmittgen, T. D. Analysis of relative gene expression data using real-time quantitative PCR and the 2(-Delta Delta C(T)) Method. *Methods* **25**, 402–408 (2001).
80. Zhang, H. *et al.* Replication of murine mitochondrial DNA following irradiation. *Adv. Exp. Med. Biol.* **645**, 43–48 (2009).
81. Dona, A. C. *et al.* Precision high-throughput proton NMR spectroscopy of human urine, serum, and plasma for large-scale metabolic phenotyping. *Anal. Chem.* **86**, 9887–9894 (2014).
82. Hoch, J. C. *et al.* Biological Magnetic Resonance Data Bank. *Nucleic Acids Res.* **51**, D368–D376 (2023).

83. Wishart, D. S. *et al.* HMDB 5.0: the Human Metabolome Database for 2022. *Nucleic Acids Res.* **50**, D622–D631 (2022).

84. Stewart, S. A. *et al.* Lentivirus-delivered stable gene silencing by RNAi in primary cells. *RNA* **9**, 493–501 (2003).

85. Sancak, Y. *et al.* EMRE is an essential component of the mitochondrial calcium uniporter complex. *Science* **342**, 1379–1382 (2013).

86. Percie du Sert, N. *et al.* The ARRIVE guidelines 2.0: Updated guidelines for reporting animal research. *PLoS Biol.* **18**, e3000410 (2020).

87. Chilibroste, S. *et al.* Preclinical Evaluation of LVR01 Attenuated Salmonella as Neoadjuvant Intralesional Therapy in Combination with Chemotherapy for Melanoma Treatment. *J. Invest. Dermatol.* **142**, 1435-1443.e2 (2022).

88. Patterson, L. H. & Murray, G. I. Tumour cytochrome P450 and drug activation. *Curr. Pharm. Des.* **8**, 1335–1347 (2002).

Author contributions

J.M. contributed to the experimental design and acquired and analyzed most of the data. C.Q. conceived the study, designed and analyzed most of the experiments. JM and CQ provided funding and wrote the manuscript. D.T. obtained the plasmids, prepared lentiviral particles, and contributed to the animal experiments. A.L. and R.D. contributed to the design, acquisition, and analysis of the proteomic data. M.M. contributed to the design of the animal model, supervised and analyzed the animal experiments. R.M-K. and M.R-T. contributed to the design and implementation of the CRISPR/Cas9 system for *Abat* knockout. M.T., C.P., and J.G. contributed to the design and performed the experiments with ^{223}Ra. I.M. and G.G. performed and analyzed the SA-beta-galactosidase experiments and contributed to the oxygen consumption rate and doxorubicin experiments. G.A., A.L-R., and G.M. designed,

performed, and analyzed the NMR-based metabolite measurements. E.M. contributed to the microscopy experiments. R.F. and M.A.D. designed and performed the GSEA and *Abat* gene promoter analyses. P.C. and M.B-F. performed cell sorting of mtEGFP-expressing cells. N.D.I. contributed to the SCENITH experiments. All authors reviewed and approved the final version of the manuscript.

Data availability

The mass spectrometry proteomics data generated in this study have been deposited in the ProteomeXchange Consortium via the PRIDE partner repository with the dataset identifier PXD083906. The NMR data generated in this study have been deposited in Mendeley Data (https://doi.org/10.17632/4hrt5wx6jb.1). All other datasets generated and/or analyzed during the current study are available from the corresponding author upon reasonable request.

Reviewer access to the proteomics dataset is available through the project accession PXD083906 using the reviewer token OcDpS4o7XBKc.

Acknowledgements

We thank Dr. Toren Finkel and Dr. Jie Liu for their helpful suggestions.

Funding

Comisión Sectorial de Investigación Científica (CSIC) (CSIC I+D 2020 ID 424 and CSIC Grupos I+D 2022) to CQ. Programa de Desarrollo de las Ciencias Básicas (PEDECIBA) (Montevideo, Uruguay) to CQ and JM. ANII (POS_NAC_2015_1_109506) and Comisión Académica de Posgrados (CAP) UdelaR to JM. Espacio Interdisciplinario Centros, Universidad de la República (UdelaR; Montevideo, Uruguay) to CQ and JM. Fondo Carlos Vaz Ferreira, (FVF/2021/060), Dirección Nacional de Innovación, Ciencia y Tecnología (DICYT) to JM.

Supplementary Files

This is a list of supplementary files associated with this preprint. Click to download.

- DatafileS3VenndiagramSenCTRL.xlsx
- DatafileS7SRXresultsfileABAT.xlsx
- DatafileS6CRISPROfftargetsSequencing.xlsx
- DatafileS4VolcanoPlotCtrlvsSen.xlsx
- DatafileS2GOCellularComponent.xlsx
- DatafileS5GSEAanalysis.xlsx
- DatafileS1Proteinsfoundin4replicatesofeachcondition.xlsx
- SupplementaryfileUncroppedWesternblots.pdf
- Supplementaryfiguresandmaterialsfinal.pdf